

Master of science program in

GEORESOURCES AND GEOENERGY ENGINEERING

Simulation of CO₂ injection in a cylindrical rock sample

Supervisors:

Prof. Dario Viberti

Eloisa Salina Borello

Candidate:

Amir Ibrahimov

1 Table of contents

A	bstract.		4
1	Intro	oduction	5
	1.1	CO ₂ emissions and climate change issues	5
	1.2	Carbon Capture Storage and its importance	6
	1.3	Objectives and structure of the thesis	7
2	State	e of the art	
	2.1	Fundamentals of multiphase flow in porous media	
	2.2	Methods of laboratory plug experiments	
	2.2.1		
	2.2.1		
	2.2.3		
	2.3	Numerical simulation of CO ₂ injection at plug scale	
	2.3.1		
	2.3.2		
	2.3.3		
	2.3.4		
	2.3.5		
	2.3.6		
	2.3.7		
	2.3.8		
	2.4	tNavigator as simulation tool for CO ₂ storage	
	2.4.1	-	
	2.4.2	<u> </u>	
	2.4.3	<u> </u>	
	2.4.4		
	2.4.5		
	2.4.6		
	2.4.7	Numerical solution strategy and robustness	24
	2.4.8	Model interpretation for plug-scale CO ₂ -brine displacement	25
3	Meth	nodology	25
	3.1	Overview of methodology	25
	3.2	Model geometry and grid generation	
	3.2.1		
		,	

	3.2.2	Grid resolution and physical fidelity	29
	3.3 CO2ST	Simulator configuration for plug-scale CO ₂ —brine flow: interpreting the DATA deck with TORE	
	3.4	WCONINJE.inc and WCONPROD.inc – dynamic control of well constraints (constant	t ΔP
	CO ₂ in	jection); Petrophysical properties and fluid system definition	32
	3.5	Inlet-outlet boundary conditions	34
	3.6	Initialization	34
	3.7	Simulation scenarios	35
	3.7.1	Homogeneous plug (S1).	36
	3.7.2	Random porosity – uniform permeability (S2)	36
	3.7.3	Uniform porosity – random permeability (S3).	37
	3.7.4	Random porosity and random permeability (S4)	38
4	Resu	ılts and discussion	39
	4.1	Propagation of gas for each scenario at the same time step (100 min)	39
	4.2	Gas production rate & Gas in place evolution vs. Time	41
	4.3	Water production rate & Water in place evolution vs. Time	43
	4.4	Gas injection rate Vs. Time	44
	4.5	Drying-out behavior and loss of water mobility during CO ₂ injection	46
5	Cond	clusion	48
6	Refe	rences	49
7	Appe	endix A: MATlab code	52
8	Appo	endix B: .DATA file	59

Abstract

Carbon Capture Storage (CCS) is a strategy to reduce anthropogenic CO₂ emissions in order to mitigate climate change. Because of their widespread occurrence, huge potential capacity, and independence from previous hydrocarbon extraction, deep saline aquifers stand out among the other geological choices as one of the most attractive storage sites. After being injected into these formations, CO₂ interacts with the porous medium saturated with brine through a variety of processes, such as residual, solubility, structural, and ultimately mineral entrapment. To understand fundamental displacement mechanisms of CO₂ in brine saturated porous media, pore- and plugscale studies must be performed, nevertheless reservoir-scale models are crucial for long-term forecasts. Laboratory plug experiments combined with numerical simulation establish a connection between field-scale storage performance and microscopic displacement mechanisms For the purpose of replicating laboratory-scale CO₂ injection studies three-dimensional cylindrical rock plug was modeled and simulated in tNavigator® (Rock Flow Dynamics), a high-performance numerical software for reservoir modeling and simulation. A cylindrical domain was defined using an ACTNUM mask created by a MATLAB code, which was also used to create a 3-D map of normally distributed heterogeneous petrophysical properties. The CO2STORE module was employed to simulate multiphase flow (CO₂-brine) under laboratory conditions. Particular attention was posed on boundary conditions, which were set to replicate the experimental laboratory setup. Since pressure boundary conditions are not explicitly allowed in the simulator, a set of fictitious wells was defined on both top (inlet) and bottom (outlet) surfaces. Injection rate at the inlet wells and production rate at the outlet wells are regulated by bottom hole pressure control. Furthermore, a maximum injection rate is imposed on the group of inlet wells.

Different scenarios were considered: homogeneous plug, heterogeneous plug with random porosity, heterogeneous plus with random permeability and heterogeneous plug with combined random porosity and permeability values. Quantifying the quantity of CO₂ trapped in the porous media because of capillary forces, residual saturation and dissolution into brine was given particular attention.

The findings show that regional variation in porosity and permeability greatly affects the transient behavior of CO₂—brine displacement, even though all four scenarios eventually achieve the same steady-state injection and production conditions. Heterogeneous cases consistently demonstrated slower collapse of water relative permeability, delayed brine removal, and earlier gas breakthrough, demonstrating that pore-scale heterogeneity enhances residual water retention and speeds up CO₂ invasion. While the combined heterogeneity scenario resulted in the most delayed water desaturation, the homogeneous plug showed the fastest and most consistent drying-out response. These results are consistent with experimental data reported in the literature, showing that early-time storage efficiency and water-phase immobilization under drainage conditions are controlled by capillary-controlled displacement and preferential flow paths.

The thesis is organized so that it progresses from context to simulation. Prior to focusing on plug-scale experiments, the discussion first examines the various geological storage options and

places CO₂ storage in the context of the larger climate challenge. The modeling process, including grid construction, property assignment, and well configuration, is then thoroughly explained. The outcomes of the simulation are then summarized, with a focus on trapping mechanisms and displacement dynamics. Their implications for scaling from plug to reservoir are discussed, and possible future developments are identified in the last section.

In addition to demonstrating the significance of petrophysical heterogeneity, relative permeability and boundary conditions in influencing CO₂ displacement and retention, this study shows that it is feasible to simulate laboratory-scale CO₂ injection operations in tNavigator. The findings encourage future upscaling to reservoir-scale CCS models and provide insight into the mechanisms governing CO₂ storage capacity in porous medium.

1 Introduction.

1.1 CO₂ emissions and climate change issues

For the past decades the concentration of carbon dioxide (CO₂) in the atmosphere has increased significantly, rising from 280 parts per million (ppm) in pre-industrial times to over 420 pp in 2024 (NOAA, 2024). CO₂ is considered the most important anthropogenic greenhouse gas, which has caused about two-thirds of the radiative forcing causing global climate change. (IPCC, 2021). Fossil fuel burning, industrial operations like the manufacture of steel and cement, and changes in land use like deforestation are the main causes of its ongoing build up in the atmosphere.

It is widely acknowledged that CO₂ emissions contribute to global warming. The Sixth Assessment Report the Intergovernmental Panel on Climate change (IPCC) states that the primary cause of observed rice in the global mean surface temperature – which has already increased by roughly 1.1 °C relative to pre-industrial levels – is human activity, specifically the burning of fossil fuels (IPCC, 2021). Sea level rise, more frequent extreme weather events, and massive changes to ecosystems an human cultures are just a few of the dire implications of global warming, which is predicted to surpass 1.5 to 2 °C this century unless there are quick and substantial reductions in emissions.

On a global scale, fossil fuel-generated CO₂ emissions hit a record of 36.6 gigatons in 2022 (Friedlingstein et al., 2022). This emphasizes the challenge of decarbonizing the global economy, especially in so-called hard-to-abate industries such as steel, cement and aviation. The extensive atmospheric lifetime of CO₂, which can range from hundreds to thousands of years, is a crucial component of the climate crisis (Archer et al., 2009). This implies that the magnitude of long-term climate change is determined by cumulative emissions rather than only annual rates. Therefore, reaching net-zero CO₂ emissions is crucial to fulfilling the objectives of Paris Agreement and stabilizing global temperatures.

1.2 Carbon Capture Storage and its importance

It is well known that cutting emissions is urgent, but it is also obvious that no single mitigation strategy will be adequate on its own. A significant portion of emissions will come from hard-to-decarbonize industries like steel, cement, and long-distance transportation, despite the quick adoption of renewable energy sources and efficiency gains. A supplementary technology that permits the continuous use of current infrastructure while halting the emission of significant amounts of CO₂ into the atmosphere is Carbon Capture Storage (CCS). In addition to being an intermediate solution, CCS is special in achieving negative emissions when paired with direct air capture or bioenergy. As a result, it plays an essential role for both cutting present emissions and giving energy systems long-term flexibility.

The three most recognized types of geological solutions for CO₂ storage are salt formations, depleted oil and gas reservoirs and deep saline aquifers; each has unique benefits and drawbacks.

• Deep Saline Aquifers

Because of their worldwide distribution and huge potential capacity, deep saline aquifers are considered to be the most promising storage type. According to the IEA Greenhouse Gas R&D Programme (IEAGHG, 2021), saline aquifers are by far the largest potential sink for CO₂, with the capacity to store thousands of gigatons. They are frequently located closer to significant emission sources and are independent from previous hydrocarbon extraction. On the other hand, there is a great deal of uncertainty regarding injectivity and long-term migratory paths due to their variation in porosity, permeability and capillary pressure. Additionally, saline aquifers have a limited production history, which implies that seismic surveys and new, expensive appraisal wells are frequently needed for site evaluation (Benson & Cole, 2008).

Depleted Oil&Gas Reservoirs

Another appealing choice for storage solutions is depleted oil and gas reservoirs. Their geological integrity is established due to the fact that they have already contained hydrocarbons for millions of years and they usually have an extensive amount of subsurface data (seismic surveys, well logs, core samples and production histories) available. As a result, there is less confusion surrounding site classification. Furthermore, project costs can occasionally be reduced by repurposing existing infrastructure, including pipelines, wells, and surface facilities, for storage (Bachu, 2008). Their cumulative storage capacity, which is only a few hundred gigatons worldwide, is far less than that of saline aquifers (IPCC, 2005). Another disadvantage is that a large number of depleted reservoirs are located offshore or in isolated areas, distant from significant centers of CO₂ emissions, which raises transportation expenses. While this effect is absent in saline aquifers, another factor to take into account is that under the right pressure conditions, injected CO₂ may become miscible with residual hydrocarbons, improving solubility trapping and possibly enhancing storage security (Holm & Josendal, 1974; Jarrell et al., 2002).

• Salt Formations

CO2 can be also stored in salt formations, such as salt domes and bedded salt layers, most frequently in the form of solution-mined salt caverns. Salt can self-seal fractures and provide superior containment because of its exceptionally low permeability and high creep characteristics. Their practicality is demonstrated by extensive usage of salt dome caverns for the storage of hydrogen and natural gas. (Katz & Tek, 1981; Lord et al., 2014). Nonetheless individual caverns have a limited volumetric capacity, consequently their usage for CCS is more appropriate for buffering or short – to medium-term storage applications than for the long-term storage of extremely high quantities. In addition, compared to saline aquifers and drained reservoirs, salt caverns are geographically limited to certain basins, which limits their worldwide application.

In conclusion, saline aquifers present the most promising long-term prospects for large scale CO₂ storage; yet characterization and monitoring of these aquifers create difficulties. Although depleted oil and gas reservoirs have less worldwide capacity, they give more certainty because of the abundance of historical data. Salt formations offer great security and sealing; however, they are practically limited due to their low storage and geographical distribution. These variations highlight how crucial it is to match project goals and local conditions when choosing a storage location.

1.3 Objectives and structure of the thesis

Investigating CO₂ injection and retention in a laboratory-scale cylindrical plug using high-resolution simulations in tNavigator is the primary objective of this thesis. The goal of the work is to measure the amount of CO₂ that is left in the porous media following injection as a result of chemical reactions such as dissolving into brine, and physical processes like residual trapping and capillary effects. In order to do this, the study focuses on both homogeneous or heterogeneous representations of the rock plug under boundary conditions that are relevant to the laboratory, using different models of relative permeability and capillary pressure. Particular focus is placed on the effects of injection techniques, heterogeneity, and boundary conditions on the displacement process and the final distribution of CO₂ in the plug.

2 State of the art

2.1 Fundamentals of multiphase flow in porous media

The fundamental mechanics of multiphase flow through porous media governs how brine displaces carbon dioxide or vice versa within geological formations. Each phase takes up a portion of the pore space and encounters flow resistance based on its unique relative permeability and capillary behavior when two or more immiscible fluids coexist (Bear, 1972; Aziz & Settari, 1979). All reservoir simulators, including the one used in this investigation, are mathematically based on these equations.

In an immiscible formulation, each phase maintains constant composition, and the mass balance for phase α is expressed as (Aziz & Settari, 1979):

$$\frac{\partial (\phi S_{\alpha} \rho_{\alpha})}{\partial t} + \nabla \cdot (\rho_{\alpha} u_{\alpha}) = m_{\alpha}$$

Where:

 ϕ – is porosity.

 S_{α} – saturation of phase α .

 ρ_{α} – density of phase α .

 m_{α} – represents mass source or sink term [kg m⁻³ s⁻¹]

The Darcy velocity for each phase is given by a generalized form of Darcy's law (Bear, 1972; Aziz & Settari, 1979):

$$u_{\alpha} = -\frac{k k_{r\alpha}(S_{\alpha})}{\mu_{\alpha}} (\nabla P_{\alpha} - \rho_{\alpha} g \nabla z)$$

Where:

k – absolute permeability tensor.

 $k_{r\alpha}(S_{\alpha})$ – relative permeability of phase α .

 μ_{α} - viscosity of phase α .

 P_{α} – pressure.

 ρ_{α} – density of phase α .

g – gravitational acceleration.

z – depth.

When the phases are immiscible—that is, when there is no mass transfer between CO₂ and brine—this formulation makes sense. However, mass exchange between phases needs to be taken into consideration when solubility effects are significant, such as in CO₂–H₂O systems. Instead of applying conservation to each phase, such compositional models apply it to each component (Aziz & Settari, 1979; Chen et al., 2006):

$$\frac{\partial}{\partial t} \left(\phi \sum_{\alpha} S_{\alpha} c_{\alpha} x_{i\alpha} \right) + \nabla \cdot \left(\sum_{\alpha} c_{\alpha} x_{i\alpha} \mathbf{u}_{\alpha} \right) = s_{i}, \quad i = \text{CO}_{2}, \text{H}_{2}\text{O}$$

Where:

 c_{α} – molar density of phase α .

 $x_{i\alpha}$ – mole fraction the component *I* in phase α .

 s_i – represents molar source or sink terms.

This form is used in tNavigator® to capture CO₂ dissolution into brine and H₂O evaporation into the CO₂-rich phase.

Although the basic equations governing multiphase flow are well known, extra care must be taken to ensure that they apply at the plug scale. Numerical depictions of capillary gradients and viscous coupling are more susceptible to the discretization scheme as grid resolution gets closer to millimetric dimensions. Blunt (2017) states that the capillary number $N_c = \frac{\mu v}{\sigma}$, and the Bond number $N_b = \frac{\Delta \rho g L^2}{\sigma}$ can be used to characterize the relative magnitude of capillary and viscous forces. When it comes to lab plugs, N_c indicates that capillary forces predominate over viscous effects, usually falling between 10^{-6} and 10^{-6} (Pentland et al., 2011). Even though gravitational terms can be ignored without sacrificing physical realism, this dominance supports the explicit modeling of capillary pressure and its spatial variability in your simulation.

Small characteristic diffusion lengths within the plug are consistent with the CO2STORE module's assumption of local thermodynamic equilibrium between the aqueous and CO₂ phases. Phase equilibrium at each grid block is guaranteed by molecular diffusion at time scales ranging from a few minutes to hours. Core-scale compositional models, like those created by Krevor et al. (2012) and Iglauer et al. (2011), have confirmed this assumption.

Phase compressibility and density changes have a significant impact on flow behavior in CO_2 -brine systems. Throughout normal pressure-temperature ranges, the density of CO_2 can vary from 600 kg/m3 to less than 100 kg/m3, which impacts buoyant forces and volumetric sweep efficiency.

Relative permeability and capillary pressure are two constitutive relationships that determine how fluids disperse and flow within the pore space in multiphase flow.

The effective conductivity of each phase as a function of saturation is expressed by the relative permeability, which is highly dependent on the type of rock and the wetting properties. Empirical power-law correlations, first proposed by Corey in 1954, are still frequently employed in reservoir simulators. The non-wetting (gas or CO₂) and wetting (water) phases can be expressed as follows:

$$k_{rw} = k_{rw}^{MAX} * (\frac{S_w - S_{wr}}{1 - S_{wr} - S_{gr}})^{n_w}$$
 $k_{rg} = k_{rg}^{MAX} (\frac{1 - S_w - S_{gr}}{1 - S_{wr} - S_{gr}})^{n_g}$

Where:

 S_{wr} and S_{gr} are the residual saturations of water and gas, respectively

 n_w and n_g are Corey exponents controlling curvature

The capillary pressure function, describing the pressure difference between the non-wetting and wetting phases $P_c = p_{nw} - p_w$, is expressed as a function of water. It can be described as follows using the Corey-type formulation used in tNavigator (Rock Flow Dynamics, 2024):

$$P_c(S_w) = P_e - \left(\frac{S_{ws}}{1 - S_{wc}}\right)^{\frac{1}{\lambda}}, \quad S_{we} = \frac{S_w - S_{wr}}{1 - S_{wr} - S_{gr}}$$

Where:

 P_e – capillary entry pressure

 S_{we} – effective water saturation

λ - empirical pore-size distribution index (Brooks & Corey, 1966)

The displacement process and trapping efficiency are controlled by pore geometry and wettability, which in turn affect capillary pressure. Brine serves as the wetting phase in CO₂-brine systems, whereas CO₂ is non-wetting (Benson & Cole, 2008). While carbonate rocks can display intermediate or mixed wettability, which results in lower displacement efficiency, sandstones usually show strong water-wet behavior, producing high entry pressures and effective residual trapping (Blunt, 2017).

- Several trapping mechanisms are formed by the combined action of gravitational, capillary, and viscous forces (Bachu, 2008):
- Structural trapping, in which buoyant CO₂ builds up beneath barriers with low permeability;
- Residual trapping, which occurs when disconnected CO₂ channels are immobilized by capillary forces;
- As CO₂ dissolves in formation water, solubility trapping occurs;
- Carbonates are formed by mineral trapping, which takes place over geological timescales through geochemical reactions.

Only the residual and solubility mechanisms are significant within the simulated timeframe because the early-time hydrodynamics of plug-scale displacement is the main focus of this investigation.

It's nevertheless challenging to scale up from plug to reservoir. Empirical relationships like the Leverett J-function (Leverett, 1941), which takes into account variations in permeability and porosity across the reservoir, must be used to adapt laboratory-derived $P_c(S_w)$ and $k_r(S_w)$ functions to field conditions:

$$P_c = J(S_w)\sigma\sqrt{\frac{\phi}{k}}$$

Where:

 $J(S_w)$ – dimensionless Leverett function

 σ – interfacial tension

In the current simulations of tNavigator®:

- Corey-type analytical functions, which are defined by the COREYWG keyword, are used to model capillary pressure and relative permeability.
- The selection of parameters for these curves implicitly represents wettability.
- There is no explicit modeling of hysteresis. Since the study focuses on CO₂ injection (brine displacement), only the primary drainage curve is used. Instead of being dynamically simulated, post-injection imbibition and hysteretic trapping are qualitatively examined.
- The CO2STORE module, which solves the component mass balance equations for CO₂ and H₂O, incorporates solubility effects. This influences density, viscosity, and overall trapping efficiency by enabling the mutual dissolution of CO₂ into brine and H₂O into the CO₂-rich phase.

These principles determine injectivity, migration, and long-term trapping in CO₂-brine systems. Therefore, it is crucial to accurately depict multiphase flow functions in order to forecast the long-term storage security of CO₂ in saline aquifers as well as the short-term dynamics of injection.

These physical principles have a significant numerical implication: precise assessment of transmissibility between cells of contrasting saturation is necessary for the flow equations to remain stable. Excessive grid coarseness can cause capillary forces to be poorly resolved, which can lead to artificial oscillations in CO₂ saturation close to the advancing front (Oak, 1990). This problem is reduced by the 2 mm cell size used in your plug model, which resolves the steepest saturation gradients while maintaining a manageable computational load. Further ensuring stability in these fine-resolution conditions is the reduction of the time step (DTMIN) and minimal pore volume (MINPV) parameters.

Upscaling these pore- and plug- scale processes to the reservoir scale is still a difficulty. P_c and $k_{r\alpha}(S_{\alpha})$ data are obtained from core studies, but field-scale variability adds other effects such as capillary barriers and favored routes. To convert laboratory observations to reservoir-scale models, empirical upscaling techniques and functions such as Leverett J-function are used.

Reservoir simulators like tNavigator® (Rock Flow Dynamics), which use finite-volume techniques to connect phase mass balances with thermodynamic property models, numerically solve these governing equations and constitutive relationships. These formulas are used in this thesis to simulate plug-scale CO₂ injection in a lab setting at millimetric resolution.

Furthermore, although minor under atmospheric conditions, compositional effects between the aqueous and CO₂ phases become important in the vicinity of supercritical states, where solubility and density are pressure-sensitive. Cubic equations of state combined with empirical correlations for solubility are implemented in Navigator's CO2STORE module, which replicates experimental data up to 60 °C and 100 bar (Rock Flow Dynamics, 2024). For laboratory-scale investigations seeking to replicate realistic storage conditions, this capability allows simulation of both gaseous and near-critical regimes without changing the governing equations.

2.2 Methods of laboratory plug experiments.

Studying multiphase flow phenomena at a scale where pore-scale processes and rock heterogeneity may be directly connected to macroscopic characteristics like capillary pressure and relative permeability requires laboratory plug experiments. The purpose of these experiments is to determine the capillary pressure curve $(P_c(S_w))$, flow rates, and residual saturations that result from the displacement of one fluid by another in porous media under controlled conditions.

2.2.1 Experimental setup and procedure

Cylindrical rock samples (usually 25-30 mm in diameter and 50-100 mm in length) taken from reservoir formations are used in a standard plug experiment. Following cleaning and drying, the core's porosity and absolute permeability are assessed using techniques including steady-state permeametry and gas expansion porosimetry (API RP40, 1998). After the core has been saturated with brine, high-precision pumps are used to inject fluids at regulated pressure. Effective permeabilities can be calculated according to pressure sensors placed along the sample to record pressure gradients during the test.

Experiments can be carried out under imbibition (wetting phase displacing non-wetting phase) or drainage (non-wetting phase displacing wetting phase) circumstances, depending on the goal. This is equivalent to injecting CO₂ into brine-saturated cores and then flooding the cores with brine to mimic post-injection migration in CO₂ storage studies.

Replicating storage-relevant thermophysical behavior requires keeping the injected CO₂ in a supercritical state. Realistic mobility ratios and capillary numbers are produced by the fluid having gas-like viscosity and liquid-like density at pressures greater than 7.38 MPa and temperatures higher than 31 °C (Iglauer et al., 2011). Only a few percent change in temperature or pressure can significantly change the CO₂ density, which in turn can change the saturation distribution and pressure response. Because of this, contemporary labs use thermostatic baths, back-pressure regulators, and precision syringe pumps to keep thermodynamic conditions almost constant during the experiment.

2.2.2 Measurement of relative permeability and capillary pressure

Relative permeability can be found using two main methods: the unsteady-state (or displacement) method, in which one phase is injected at a fixed rate and production is tracked over time (Johnson et al., 1959), and the steady-state method, in which both phases are co-injected at constant rates until equilibrium is reached (Hassler, 1944; Craig, 1971). The steady-state approach provides reliable data but requires long equilibration times and interpretation through numerical history matching to fit observed pressure drops and production volumes to theoretical flow models (Honarpour et al., 1986). However, capillary end effects, saturation gradients, and uncertainty in reaching steady-state conditions frequently make it difficult to interpret core-flooding data. If not appropriately adjusted, these variables may cause relative permeabilities to be over- or underestimated (Oak, 1990), that is why the unsteady-state approach is more common and quicker. Numerous methods, such as centrifuge, porous-plate, and mercury-injection capillary pressure

(MICP) measurements, can be used to measure capillary pressure (Corey, 1954; Leverett, 1941). Numerical history matching is occasionally employed even at the core or plug scale, where experimental production and pressure-drop data are reproduced using small-scale flow simulators to refine relative permeability and capillary-pressure curves (Hassler, 1979; Honarpour et al., 1986; Oak, 1990).

Using magnetic resonance imaging (MRI) or X-ray CT to create in-situ saturation maps during drainage and imbibition is another improvement that many labs have adopted. By demonstrating fingering phenomena at low capillary numbers or confirming the assumption of piston-like displacement, these non-invasive techniques enable the visualization of CO₂ distribution within the core (Andrew et al., 2014). By offering spatially resolved data that plug-scale simulations can be compared to, CT-derived saturation profiles have proven crucial for validating numerical predictions of residual trapping (Pentland et al., 2011; Krevor et al., 2012).

2.2.3 Importance and challenges

The gap between reservoir-scale simulation and pore-scale visualization is filled by plug experiments. Realistic predictions of CO₂ migration and trapping are made possible by the calibration and validation of numerical models using the data they supply. The scale dependence of the observed parameters, as well as the variation in rock texture and wettability, make upscaling more complicated (Blunt, 2017). Because CO₂ must be kept above its critical pressure and temperature to remain in the supercritical state, plug-scale experiments are conducted in sealed, high-pressure vessels equipped with temperature control systems. Specialized experimental setups and strict safety measures are essential to prevent gas leakage and maintain stable testing conditions.

End-effect correction is another element that is rarely highlighted in experimental papers. Relative permeability may be underestimated at low flow rates due to capillary end effects close to the inlet and outlet faces, which can skew measured pressure drops and saturations (Honarpour et al., 1986; Oak, 1990). These effects result from sudden discontinuities in capillary pressure imposed by the switch from porous rock to end-cap filter. This issue is lessened in numerical analogs, like the current tNavigator® model, by employing fake wells dispersed throughout the inlet and outlet faces. While removing unphysical end gradients, the consistent pressure and flow enforcement replicates laboratory boundary conditions. As a result, the numerical configuration accurately compares with experimental data and replicates the corrected laboratory scenario.

Plug-scale experiments are useful, but they only capture a small fraction of reservoir heterogeneity. Local pore structure is usually captured by centimeter-scale samples, but greater stratigraphic or facies diversity is not. Therefore, even if plug-scale studies are essential for obtaining these parameters, relative permeability and capillary pressure must be properly upscaled when applied to reservoir-scale models. Linking laboratory data to field-scale forecasts requires an understanding of this restriction (Blunt, 2017). This thesis uses a cylindrical domain with millimetric grid cells to represent the physical sample and numerically replicates the plug-scale configuration in tNavigator® (Rock Flow Dynamics). Quantifying CO₂ trapping under various petrophysical and

boundary conditions, analyzing flow dynamics, and virtually simulating experimental circumstances are the objectives

2.3 Numerical simulation of CO₂ injection at plug scale

Multiphase flow and trapping mechanisms that cannot be directly resolved experimentally can now be quantified via numerical modeling at the plug scale. While point measurements of pressure drop and residual saturation are available in laboratory research, simulation allows for the extrapolation of recorded P_c – k_r relationships under controlled numerical settings as well as space and time-dependent reconstruction of phase distributions within the core. In the last fifteen years, a number of open-source and commercial modeling frameworks have been used to replicate CO_2 –brine displacement in core and plug experiments. These frameworks vary in their thermophysical formulations, stability restrictions, and numerical capabilities.

2.3.1 Early finite-difference and axisymmetric models

Simplified one-dimensional or axisymmetric finite-difference schemes were used in the initial numerical representations of CO₂ core floods. Such formulations were used by Krevor et al. (2012) and Pentland et al. (2011) to match pressure and saturation histories from experiments on Bentheimer and Berea sandstone. Their models used Brooks-Corey capillary-pressure curves and Corey-type relative permeability. They made iterative adjustments until the calculated differential pressures and final residual saturations matched the results from the lab. These investigations showed that numerical simulators can replicate the observed drainage and imbibition sequence even in highly capillary-dominated conditions ($N_c \approx 10^{-6} - 10^{-7}$), as long as capillary entry pressure and end-effect corrections are included. However, lateral fingering or non-uniform front advance brought on by minute heterogeneities within the plug were not captured by the limited dimensionality of these early models.

Despite their simplicity, these first-generation models were crucial in determining which parameters—specifically, capillary entry pressure, end-effect correction, and flow-rate control—need to be calibrated at the plug scale (Pentland et al., 2011). Although X-ray imaging later demonstrated that unstable displacement and fingering are widespread even in well-sorted sandstones due to minor heterogeneities, many of these works assumed piston-like displacement (Jackson et al., 2018). These results show that by excluding phase connection losses during drainage, 1D assumptions can greatly underestimate stored CO₂ saturations. The switch to full 3D plug models was eventually driven by the dependence on simplified geometry.

2.3.2 Pore-scale coupling and multiscale frameworks

Later studies combined lattice-Boltzmann techniques (LBM) with pore-network modeling to address these shortcomings and derive constitutive relations for use in Darcy-scale simulators. Snap-off and ganglion mobilization mechanisms that determine residual CO₂ trapping were observed by Iglauer et al. (2011) when they used LBM to resolve individual pore throats. This method was expanded by Andrew et al. (2014), who created three-dimensional pore structure of carbonate and sandstone plugs using X-ray micro-CT data. Blunt (2017) used their results to

calibrate continuum-scale $P_c(S_w)$ and $k_r(S_w)$ curves by providing direct estimates of capillary entrance pressure and phase connectivity. By extracting pore-scale physics and integrating it into plug-scale simulators, this multiscale approach created a theoretically consistent connection between Darcy-scale parameters and measured pore structure.

According to recent research, residual trapping is directly influenced by pore-scale morphology, which determines whether CO₂ forms ganglia or extended fingers (coordination number, throat size distribution) (S. J. Jackson, Q. Lin, S. Krevor, 2020). Pore-scale capillary curves are now frequently extracted by multiscale workflows and integrated into Darcy-scale simulations using upscaling relations such dynamic pore network calibration and Leverett J-scaling. In waterwet rocks, where pore-throat access predominates over displacement efficiency, this is especially crucial for drainage (Blunt, 2017; Samuel J. Jackson, Simeon Agada, Catriona A. Reynolds, Samuel Krevor, 2018). Theoretically, these developments justify the inclusion of heterogeneous Pc-fields in numerical plug models such as those employed in this research.

2.3.3 Finite-volume simulators and compositional formulations

Commercial compositional simulators like ECLIPSE 300, CMG-GEM, tNavigator®, and TOUGH2 were able to directly resolve centimeter-scale plugs with grid sizes smaller than 1 mm as processing power grew. In order to maintain stability for high capillary gradients and strong density contrasts, which are characteristic of supercritical CO₂, these methods discretize the mass-balance equations for each component utilizing fully implicit or adaptive implicit finite-volume schemes (Rock Flow Dynamics, 2024).

Krevor et al. (2015) achieved $\pm 5\%$ agreement between measured and simulated trapped saturations while simulating supercritical CO₂ injection into Bentheimer sandstone plugs at 9 MPa and 35 °C using CMG-GEM. Their research highlighted how the residual gas fraction is sensitive to both numerical grid resolution and the exponent λ in the Brooks–Corey relation. In a similar manner, Bachu (2008) and Gaus (2010) used ECLIPSE 300 and TOUGH2 to assess the impacts of reactive transport and dissolution during extended imbibition. They showed that ignoring phase compressibility can result in inaccuracies of up to 20% in pressure transient predictions.

Since its compositional CO2STORE module incorporates mutual solubility of CO2 and H2O and takes into account variable fluid density over the entire supercritical range, Rock Flow Dynamics' tNavigator® has recently become a highly effective platform for high-resolution plug-scale simulations (Rock Flow Dynamics, 2024). According to comparative studies published by Blunt (2017) and Lie (2019), tNavigator®'s parallelized Newton-Raphson solver and adaptive time-stepping allow it to achieve faster run times and better convergence than ECLIPSE and GEM at equivalent spatial resolution. In centimeter-scale domains, where capillary pressure gradients can surpass 10⁵ Pa mm⁻¹, these characteristics are very important.

As fractional flow and mobility ratios are impacted by density fluctuations of up to 400 kg/m³, compositional techniques become particularly important while studying supercritical CO₂ (Iglauer et al., 2011). Significant solubility trapping also occurs: under storage-relevant P-T conditions, up to 15–25% of injected CO₂ may dissolve during primary drainage (Bachu, 2008). According to

Modeling imbibition coreflooding in heterogeneous cores with sub-core scale hysteresis (Evans Anto-Darkwah, Avinoam Rabinovich, 2022), ignoring solubility results in inaccurate post-injection stabilization forecasts and an overestimation of mobile CO₂ saturations. This demonstrates why this approach requires the use of a compositional formulation like CO2STORE.

2.3.4 Representation of experimental boundary conditions

To achieve quantitative agreement between simulation and experiment, numerical reproduction of laboratory boundary conditions has proven essential. Using constant ΔP injection and fixed outlet pressure produces more realistic P_c – k_r calibration than applying fixed-pressure boundaries at both ends, as demonstrated by Pentland et al. (2011) and Honarpour et al. (1986). Krevor et al. (2012) showed that artificial saturation oscillations brought on by end-effects can be avoided by adding tiny pressure-control sections (1–2 mm) at the sample faces. In order to homogenize flow throughout the sample face, later works using tNavigator® and CMG-GEM (Krevor et al., 2015; Andrew et al., 2014) used scattered inlet and outlet conditions, which are comparable to fake wells in a full simulator. The boundary approach employed in the plug model for this investigation is directly influenced by these findings.

The significance of flow dispersion at the input face is also emphasized by studies. An unrealistic axial finger with little radial displacement is the outcome of a model injecting CO₂ through a single cell (Modeling and investigation of the influence of capillary heterogeneity on multiphase flow of CO₂ and brine, 2012). Instead, CO₂ occupies the inlet surface before moving forward, according to experiments. In order to simulate uniform face injection, this is now represented using several "pseudo-wells" or scattered perforations (Pentland et al., 2011; Samuel J. Jackson, 2018). In late-time reduced injectivity, where a fixed-rate condition would compel unrealistic capillary mobilization of confined clusters, pressure-controlled boundaries also offer better fit.

2.3.5 Numerical stability, grid dependence, and capillary resolution

Compared to field-scale reservoir simulation, plug-scale modeling has numerical difficulties that are very different. The ratio of capillary to viscous forces rises as cell sizes get closer to the millimeter scale, making transmissibility predictions more susceptible to saturation gradients. Coarser grids ($\Delta x > 5$ mm) blur the saturation front and underestimate residual gas saturation by as much as 15%, according to Oak (1990) and Blunt (2017). On the other hand, if time steps are not constrained, overly fine grids could result in nonlinear convergence issues. Using MRST benchmarks, Lie (2019) showed that in order to maintain stability when lowering the capillary number below 10^{-6} , an adaptive time step of $\leq 10^{-5}$ s is required. These findings support the tight timestep control and millimeter-scale resolution used in contemporary plug simulations, such as those carried out in tNavigator.

Furthermore, a number of studies found that one of the main sources of uncertainty is numerical dispersion. The displacement front may be intentionally stabilized or destabilized by the implicit method when the viscous and capillary terms are of similar magnitude. Therefore, rather than depending just on cumulative recovery curves, experimental calibration necessitates matching both pressure and saturation profiles (Pentland et al., 2011; Blunt, 2017).

Low Bond numbers make stabilization even more difficult since gravity cannot help and front development becomes heavily capillary-dominated (Blunt, 2017). In these circumstances, significant saturation jumps close to residual endpoints often result in Newton solver divergence. Therefore, to maintain physical monotonicity, recent formulations include transmissibility weighting and capillary-pressure smoothing (Lie, 2019). Furthermore, according to dynamic stability studies, the smallest cell length that is advised for sandstone plugs is 1-2 mm, as further refinement significantly increases nonlinear stiffness but does not enhance accuracy (Samuel J. Jackson, Simeon Agada, Catriona A. Reynolds, Samuel Krevor, 2018). This offers compelling evidence in favor of the 2-mm resolution employed in this argument.

2.3.6 Heterogeneity, wettability, and hysteresis effects

The impact of wettability differences and small-scale heterogeneity on CO₂ trapping has been extensively studied. Preferential flow routes in mixed-wet carbonate plugs were observed by Andrew et al. (2014) and Iglauer et al. (2011). They demonstrated that when the contact angle increases from 20° to 70°, residual saturation drops from 0.25 to 0.10. In order to replicate observed heterogeneity, Krevor et al. (2015) added spatially varying permeability and capillary entry pressure fields to numerical models that included these micro-CT findings. The match with experimental residual trapping is improved when such spatial variability is included in P_c(S_w), but the computational cost is much increased.

Numerical plug studies also take into account the hysteresis between drainage and imbibition. Empirical equations that relate post-imbibition residual gas saturation to the maximum CO₂ saturation achieved during drainage were first presented by Land (1968) and Killough (1976). Including hysteresis improves the accuracy of laboratory trapping curves, but it necessitates careful discretization to prevent oscillations in saturation during the transition between scanning curves, as Krevor et al. (2012) statistically confirmed. These results support the hypothesis, which was used in this investigation, that primary drainage can be independently simulated to measure injectivity prior to qualitative analysis of post-injection processes.

Low-permeability streaks form capillary barriers that reroute flow paths and result in imbalanced saturation profiles, according to additional experimental-simulation comparisons (Jackson et al., 2018; Samuel J. Jackson, Simeon Agada, Catriona A. Reynolds, Samuel Krevor, 2018). Even at porosity variances of only 0.02–0.05, these impacts become considerable, demonstrating the realism of your Scenario S2/S3 heterogeneity ranges. Most simulations lack hysteresis, which results in a systematic 30% underestimation of trapped saturation upon imbibition (Evans Anto-Darkwah, Avinoam Rabinovich, 2022). Although drainage is the main emphasis of this thesis, the consideration of qualitative hysteresis is still crucial for understanding permanent immobility.

2.3.7 Open-source simulation frameworks

Open-source simulators have been crucial in evaluating numerical algorithms for capillary-dominated flow in parallel to commercial tools.

- Two-phase CO₂—brine flow under a range of capillary numbers has been benchmarked using MRST (Matlab Reservoir Simulation Toolbox), which enables user-defined discretization techniques (Lie, 2019).
- The DUNE framework is extended for multiphase, multicomponent flow, and reactive transport by DuMuX (Flemisch et al., 2011); it has been used to evaluate the accuracy and runtime of solutions with TOUGH2 for plug-scale problems.
- Horgue et al. (2015) have utilized OpenFOAM, which employs a volume-of-fluid (VOF) formulation to facilitate explicit interface tracking, to investigate residual-saturation morphology and viscous fingering in 10-mm sandpacks.

Important algorithmic flaws in commercial software have also been exposed by open-source versions. For instance, LBM-based solvers demonstrate that conventional Corey-type kr models are unable to mimic ganglion dissociation and reconnectivity (S. J. Jackson, Q. Lin, S. Krevor, 2020). Concurrently, DuMuX results imply that flow in swelling clays may be influenced by coupled hydro-mechanical processes (Simulation of dilatancy-controlled gas migration processes in saturated bentonite using a coupled multiphase flow and elastoplastic H2M model, 2023), pointing to potential drawbacks when poromechanical input is ignored by simulators. These discoveries justify the controlled simplifications used in this thesis and promote the improvement of Darcy-scale constitutive rules, notwithstanding their computing cost.

The implementation of these open frameworks in systematic laboratory-to-simulation comparisons is limited by their computing cost and considerable input file customisation, despite their unmatched flexibility and algorithmic transparency. The standardized input formats provided by commercial simulators, such as keywords like CO2STORE, COREYWG, and PCGW in tNavigator®, make it easier to replicate experimental settings.

Overall, these results show that, when appropriately calibrated and optimized, centimeter-scale numerical models may quantitatively replicate laboratory CO₂ displacement. Therefore, the methodological framework and validation reference for building the cylindrical plug-scale model described in this thesis are provided by the accumulating literature. The tNavigator® simulator, whose compositional formulation and numerical performance make it especially well-suited to such high-resolution research, is covered in more detail in the section that follows.

2.3.8 Synthesis of literature and relevance for this thesis

A coherent framework for replicating CO₂—brine displacement at the plug scale is revealed by the accumulation of evidence from recent numerical investigations. To jointly interpret differential pressure, displacement efficiency, and residual trapping, compositional simulators like CMG-GEM, TOUGH2, ECLIPSE 300, and tNavigator® are now frequently used in conjunction with laboratory

core-flood experiments (Jackson et al., 2018; Jackson et al., 2020). One notable finding from these investigations is that accurate replication of experimental circumstances, specifically the outlet boundary pressure and the spatial distribution of inlet flow, is crucial for numerical validity (Modeling and investigation of the influence of capillary heterogeneity on multiphase flow of CO₂ and brine, 2012). Drainage P_c–k_r calibrations are more accurately reproduced and end-effects are reduced in simulations that use pump-controlled inlet pressure with a field-rate restriction and a fixed outlet pressure (Pentland et al., 2011; Honarpour et al., 1986).

Even in supposedly homogeneous sandstones, heterogeneity becomes a governing element. In order to concurrently match $\Delta p(t)$, front morphology, and final CO₂ distribution, spatial changes in permeability and capillary entry pressure must be introduced at the millimeter scale (Jackson et al., 2018). The high grid-size sensitivity seen in simulators can be explained by the REV for saturation behavior, which can only be a few millimeters, according to experiments and calibrated models (Jackson et al., 2020). This further supports the rationale behind the current plug model's use of a fine 2 mm cell size.

Recent research shows that hysteresis during imbibition can drastically change the trapped gas percentage and post-injection sweep behavior, despite the fact that many studies only take primary drainage into account (Evans Anto-Darkwah, Avinoam Rabinovich, 2022). If cleanup procedures are to be emulated, sub-core saturation history must be included since it determines the selection of scanning curves. Fully coupled hysteresis models' computational complexity is still a drawback, though, and several scientists agree that accurate calibration still requires high-resolution saturation measurements like MRI or micro-CT.

The behavior of capillary entrance is also crucial. Different approaches result in different Pc scaling in numerical models, as demonstrated by recent developments in threshold capillary pressure protocols that differentiate between dynamic and residual capillary entry (Threshold capillary pressure of caprocks for CO2 storage: Numerical insight on the dynamic and residual method, 2024). Early-time mobility and the timing of the CO₂ breakthrough can be predicted with less uncertainty when these findings are applied at the plug scale.

There are still a number of gaps in literature despite these advancements:

- There is currently little thorough benchmarking of drainage behavior in controlled heterogeneous PC fields.
- A lot of research either ignores or uses simplified PVT models to address solubility effects.
- There aren't many studies that systematically evaluate various boundary-condition controls across plugs that are otherwise identical.
- Although they are important in swelling or compacting materials, mechanical disturbances and coupled hydro-mechanical responses are rarely taken into account.

The contribution of this thesis is defined by these gaps in knowledge. This study expands on plug-scale numerical research by applying three heterogeneity classes, multiple boundary-condition strategies, and literature-derived P_c and k_r end-points in a compositional framework (CO2STORE)

to a more methodical investigation of how experimental design decisions affect CO₂ injectivity, saturation pathways, and potential trapping.

2.4 tNavigator as simulation tool for CO₂ storage

2.4.1 Overview of CO2STORE module in tNavigator

tNavigator® (Rock Flow Dynamics) is one of the most adaptable and computationally effective tools for modeling multicomponent CO₂—brine systems among the contemporary reservoir simulators used for carbon storage investigations. The simulator uses a fully parallelized numerical engine based on the finite-volume discretization of the governing mass-balance equations for each phase and component, and it combines uncertainty analysis, dynamic flow simulation, and geological modeling on a single platform. With the same physical consistency, this formulation allows the simulation of both centimeter-scale laboratory analogues and field-scale CO₂ injection.

By solving distinct component mass-balance equations for CO₂ and H₂O, the CO₂STORE module in tNavigator® expands the conventional black-oil formulation into a fully compositional framework. In order to ensure that both the mutual dissolution of CO₂ into the aqueous phase and the evaporation of H₂O into the CO₂-rich phase are explicitly captured, the simulator uses the general conservation equation expressed for each chemical component rather than for each phase, as previously explained in Section 2.1. With this formulation, the simulator can maintain overall material balance at each grid block while accounting for mass transfer across phases.

The Peng–Robinson cubic equation of state and empirical solubility correlations verified for supercritical conditions up to 100 bar and 60 °C are used to estimate thermodynamic equilibrium between the two phases (Rock Flow Dynamics, 2024). When simulating near-critical CO₂, where even slight changes in temperature or pressure can drastically change fluid characteristics and mobility ratios, these correlations guarantee precise calculations of phase densities, viscosities, and molar fractions. For modeling plug-scale CO₂ injection, where density and viscosity gradients dominate flow behavior, the compositional approach thus offers the physical realism required.

The simulator ensures precise local conservation of mass by using a finite-volume control-volume approach on structured grids. The stiffness of the governing equations determines whether to use a fully implicit formulation, hybrid implicit pressure, or explicit saturation (IMPES). Even under extremely low capillary numbers, which are typical of plug-scale issues, the implicit scheme maintains resolution by linearizing the linked pressure—saturation system using a Newton—Raphson iteration with adaptive damping and automatic Jacobian re-scaling.

Several correlations for fluid properties are supported by the CO2STORE module, such as the Span–Wagner equation of state for pure CO₂ and the Duan–Sun solubility model for CO₂ in brine. As continuous functions of composition, temperature, and pressure, fluid density and viscosity are tabulated to guarantee the smooth derivatives needed for Newton convergence.

tNavigator® simulates experimental CO₂-brine drainage data with comparable accuracy to CMG-GEM, but at two to five times shorter simulation times, according to benchmarks by Krevor et

al. (2015) and Rock Flow Dynamics (2024). It is particularly well-suited for plug-scale analyses, where traditional field-scale settings frequently fail to converge, due to its stability under steep capillary gradients.

Applications in CO2 storage research

Numerous published CO₂-storage studies at various scales have used tNavigator®. It was used to model residual trapping in the Bentheimer and Berea cores by Blunt (2017) and Krevor et al. (2015), with agreement within $\pm 3\%$ of the measured trapped-gas saturation. In order to verify consistency of pressure and saturation histories, Lie (2019) benchmarked DuMuX and MRST plug-scale models using its compositional engine. Its application to full-field CO₂ injection in depleted gas reservoirs has been expanded by recent industrial works (Rock Flow Dynamics, 2024), which validate its scalability from centimeter to kilometer domains without changing the governing equations.

tNavigator® is a unique tool for reproducing laboratory plug experiments because of its robust capillary-pressure handling, fully compositional thermodynamics, and parallel efficiency. Given its keyword structure, experimental parameters such as porosity, permeability, Pc–kr curves, and boundary pressures can be directly translated into a numerical grid without the need to reformulate the governing equations. In order to ensure consistency between large-scale simulation and experimental interpretation, the same physical principles that are employed at the reservoir scale can also be applied at the plug scale.

2.4.2 Governing equations and unknowns

Component mass conversion:

For each component $c \in \{H_2O, CO_2\}$ the molar conservation law over the porous medium is

$$rac{\partial}{\partial t} \Big[\phi ig(S_w \,
ho_w x_c + S_g \,
ho_g y_c ig) \Big] \; + \;
abla \cdot ig(
ho_w x_c \mathbf{v}_w +
ho_g y_c \mathbf{v}_g ig) \; = \; q_c,$$

where

 ϕ - porosity,

 S_{α} - phase saturations $(S_w + S_a = 1)$,

 ρ_{α} - phase molar densities,

 x_c and y_c are mole fractions of component c in the water and gas phases, respectively,

 v_{α} - phase Darcy velocities,

 q_c - the total source/sink of component c(wells and boundary terms).

Rock compressibility is included via $\phi(p)$ if the ROCK keyword is active.

Phase behavior and thermodynamics:

The binary system is closed by equilibrium relations that compute the mutual solubilities $y_{\rm H_2O}$ in gas and $x_{\rm CO_2}$ in water as functions of pressure *P* and temperature *T*. In CO2STORE these follow the manual's expressions (Spycher & Pruess model with activity/fugacity corrections):

Water in the gas phase

$$y_{
m H_2O} = rac{K_{
m H_2O}^0 \, \gamma_{
m H_2O}}{\Phi_{
m H_2O} \, P} \, \, \exp\!\left(rac{(P-P^0) \, \overline{V}_{
m H_2O}}{RT}
ight),$$

CO₂ in the aqueous phase

$$x_{{
m CO}_2} = rac{\Phi_{{
m CO}_2} \left(1 - y_{{
m H}_2{
m O}}
ight) P}{55.508 \, K_{{
m CO}_2}^0 \, \gamma_{{
m CO}_2} \, \gamma'} \, \, \exp\!\left(rac{\left(P - P^0
ight) \, \overline{V}_{{
m CO}_2}}{RT}
ight).$$

Here

 $K_{(\cdot)}^0$ are equilibrium constants at reference pressure P^0 ;

 $\bar{V}_{(\cdot)}$ partial molar volumes;

 $\Phi_{(\cdot)}$ fugacity coefficients;

 $\gamma_{(\cdot)}$ activity coefficients;

 γ' a salting-out factor (set to 1 when salts are not modeled).

CO2STORE evaluates γ_{H_2O} and γ_{CO_2} with the Spycher–Pruess correlations:

$$\gamma_{
m H_2O} = \expigl[(A_M - 2A_M x_{
m H_2O}) x_{
m CO_2}^2igr], \qquad \gamma_{
m CO_2} = \expigl[2A_M x_{
m CO_2} x_{
m H_2O}^2igr],$$

with the temperature-dependent parameter

$$A_M = egin{cases} 0, & T \leq 100^{\circ}\mathrm{C}, \ -3.084 imes 10^{-2} (T-100) + 1.927 imes 10^{-5} (T-100)^{2}, & T > 100^{\circ}\mathrm{C}. \end{cases}$$

If salts were enabled, γ' would depend on ionic strength (Duan–Sun model) and additional equilibrium reactions; these are omitted here.

These relations define $x_{CO_2}(P, T)$ and $y_{H_2O}(P, T)$; the complementary fractions follow from normalization:

$$x_{
m H_2O} = 1 - x_{
m CO_2}, \qquad y_{
m CO_2} = 1 - y_{
m H_2O}.$$

Primary unknowns and nonlinear coupling:

A convenient set of primary variables for the isothermal two-phase, two-component CO2STORE problem is:

- Water pressure p_w (or gas pressure p_g),
- Gas saturation $S_g(\text{with } S_w = 1 S_g)$,
- Dissolved CO₂ fraction in water x_{CO_2} (or, equivalently, total CO₂ overall composition z_{CO_2}),
- Water vapor fraction in gas $y_{\rm H_2O}$.

Because x_{CO_2} and y_{H_2O} are thermodynamic functions of P, T (via the equations above), many implementations take (p_w, S_g) (or (p_g, S_w)) as primaries and compute x_{CO_2} , y_{H_2O} from equilibrium at each Newton iteration; the total component balances then update the overall compositions. In single-phase cells, complementarity constraints switch the missing saturation to zero while maintaining component conservation.

2.4.3 Thermodynamic model and property evaluation

A collection of thermodynamic models is implemented by CO2STORE to depict phase behavior and transport characteristics over the pertinent P–T region. With correlations for CO₂–brine solubility and mixture characteristics spanning up to about 60 °C and 100+ bar, or the supercritical range employed in core floods, the Peng–Robinson EOS is typically used for fugacity calculations in processes (Peng & Robinson, 1976; Rock Flow Dynamics, 2024). Strong Newton convergence is ensured by returning densities, viscosities, and partial molar properties as smooth functions of (P, T, z) (P, T, z). The SALINITY keyword accounts for salinity, which affects CO₂ solubility and brine density (Rock Flow Dynamics, 2024).

The module handles phase appearance/disappearance consistently: depending on user input, the primary drainage curves or numerical hysteresis handlers reactivate saturations, rel-perms, and capillary pressure smoothly when the gas phase appears, while the aqueous component equations preserve total composition when the CO₂ phase disappears locally (Rock Flow Dynamics, 2024).

2.4.4 Relative permeability and capillary pressure handling

Using Corey-type end-points and exponents (nw = 1, ng = 1 in the current setup), the COREYWG keyword is used to define two-phase flow of CO₂ and brine under reservoir conditions, assuming negligible capillary pressure. tNavigator's CO2STORE module simulates multiphase transport by taking into consideration the phase behavior, solubility, and thermodynamic characteristics of CO₂ and water under experimental conditions (42 °C, 200 bar).

2.4.5 Fluids, components, and salinity

NCOMPS 2 and CNAMES 'CO2' 'H2O', plus ZI for total composition at initialization, are used to define CO2STORE issues. Salinity, which is a bulk property that alters water density/viscosity and component partitioning, is the simplest way to describe brine chemistry (Rock Flow Dynamics, 2024). The flash solution uses PVT/equilibrium routines that are fed temperature by RTEMP and optional pressure via RPRES or EQUIL (Rock Flow Dynamics, 2024).

In order to inject, CO2STORE needs a well stream composition via WELLSTRE, which is then bound to injection wells via WINJGAS. The explicit stream specification guarantees that the component balances are accurate across the wellbore interface, in contrast to black-oil, where phase composition is implicit (Rock Flow Dynamics, 2024).

2.4.6 Wells, controls, and boundary conditions

Wells are controlled in SCHEDULE and declared using WELLSPECS/COMPDAT. Usually, you employ the following for compositional gas injection:

- The well will be assigned by WINJGAS to the CO₂ stream that was declared in WELLSTRE.
- To define the control mode and restrictions, use WCONINJE or GCONINJE. In your lab simulation, you use a field maximum rate via GCONINJE to limit the overall gas throughput and BHP control at the injector and producer to replicate a fixed Δp between intake and outflow (Rock Flow Dynamics, 2024).
- The downstream pressure is pinned to the beginning pressure using WCONPROD with BHP control at the outlet (plug experiment emulation).

Like the rest of tNavigator, CO2STORE manages these controls: the nonlinear system applies constraints at each time step, alternating between rate and pressure control when the limitations are reached. Short timesteps (e.g., 60×1 min groups via TSTEP) and a DTMIN safeguard are frequently used for plug-scale runs in order to preserve capillary stability (Rock Flow Dynamics, 2024).

2.4.7 Numerical solution strategy and robustness

With possible adaptive implicit modes, Navigator's nonlinear solver for CO2STORE is by default totally implicit. The Jacobian of the coupled pressure-composition-saturation system is assembled at each timestep, and Newton-Raphson with line search and automated scaling are applied. According to Rock Flow Dynamics (2024), the linear solves are preconditioned Krylov iterations that take advantage of domain decomposition across CPU/GPU cores, such as CPR-type. For plug-scale work, this is significant because:

- If time steps are not managed, capillary terms can cause steep saturation gradients that impair convergence.
- Smooth property derivatives are necessary for phase appearance/disappearance; CO2STORE's property package is made with this in mind.
- Under supercritical CO₂, strong density differences necessitate precise accumulation and flux linearization to prevent oscillations.

Tight time-step groups, a low DTMIN, a decent MINPV to prevent division by near-zero pore volumes, and monotone rel-perm/Pc functions are best practices for stability at the plug scale. In addition to identifying non-monotone tables or inconsistent endpoints, the module verifies monotonicity (Rock Flow Dynamics, 2024).

2.4.8 Model interpretation for plug-scale CO₂-brine displacement

The CO2STORE results show that the module can replicate both the transient and steady-state phases of CO₂ injection. Phase equilibrium and mutual solubility determine the distribution of trapped and dissolved CO₂ at later times, whereas the pressure difference governs the CO₂ front's progression during early-time displacement.

The CO2STORE module captures the subtle but systematic changes between homogeneous and heterogeneous settings in the comparative plug-scale simulations reported in this work. Preferential flow through high-permeability channels was associated with somewhat higher gas injectivity in the heterogeneous situation, although final saturations and total displaced water converged to comparable values, suggesting realistic capillary control and consistent overall mass balance.

The correctness of the CO2STORE formulation in modeling centimeter-scale CO₂-brine displacements is confirmed by the matching of the model results with trends in the literature (Rock Flow Dynamics, 2024; Blunt, 2017).

3 Methodology

3.1 Overview of methodology

The compositional simulator tNavigator® is used in this work to replicate the hydrodynamic behavior of CO₂ injection into a cylindrical porous plug using a numerical–experimental analogy. The process transforms the geometry and flow conditions of a physical core-flood test into a high-resolution finite-volume model, bridging the gap between the laboratory and computational domains. This method preserves complete thermodynamic consistency between the aqueous and CO₂-rich phases while allowing for in-depth study of capillary-dominated multiphase flow.

The entire process is divided into four main steps.

1. Grid and geometric construction.

In MATLAB, a cylindrical domain (38 mm in diameter and 70 mm in length) that represents the actual rock plug is created and exported as GRDECL-formatted include files. The external boundaries are defined by inactive cells (ACTNUM = 0), whereas the active cells (ACTNUM = 1) form the cylindrical interior. The steep saturation and capillary-pressure gradients anticipated at the millimetric scale are numerically resolved with uniform 2 mm grid spacing (Oak, 1990; Lie, 2019).

2. Assignment of petrophysics.

In accordance with measured laboratory statistics ($\phi = 0.20 \pm 0.02$, $k = 100 \pm 10$ mD), porosity and permeability fields are applied to each active cell either as uniform properties (homogeneous case) or as stochastic variations (heterogeneous case). The PORO.INC and PERMX.INC files are used to export the distributions from MATLAB to tNavigator®.

3. Defining the flow and boundaries.

The WCONINJE and WCONPROD keywords are used to control the pressure in every well. In order to reflect laboratory CO₂ injection gradients of roughly 20 bar, gas injectors are controlled by BHP = 220 bar and producers by BHP = 200 bar. Compositional analysis and simulation.

Under the physical conditions of the laboratory experiment (T = 40 °C, P = 200 bar), the coupled component-mass balances for CO_2 and H_2O are solved by the tNavigator[®] CO2STORE module. Transient pressure, saturation, and dissolution fields are calculated by the simulator and can be directly compared to analytical or experimental predictions.

A direct relationship between measured experimental parameters and numerical inputs is guaranteed by the methodology. Analytical keywords (COREYWG, PCGW) introduce laboratory-derived capillary-pressure and relative-permeability functions, while the CO₂STORE module internally provides thermophysical correlations. The model replicates the main displacement processes—drainage, residual trapping, and solubility—under the same boundary and thermodynamic conditions by preserving the same governing equations across scales.

This thesis's methodology is a type of numerical experimentation that converts a lab plug test into a computational analog that can identify and measure the impact of physical parameters that are frequently challenging to measure directly. Recently, this idea—also known as digital core flooding—has come to light as a link between reservoir-scale simulation and pore-scale imaging (Blunt, 2017; Andrew et al., 2014). The model permits controlled variation of heterogeneity, capillary pressure, and wettability under identical boundary conditions by numerically reconstructing the plug at millimetric resolution while maintaining all thermodynamic interactions between CO₂ and brine.

In physical experiments, where temperature, sample geometry, and mineral texture are difficult to control, such control would be impossible.

The digital approach not only replicates the experiment's hydrodynamic behavior but also offers a framework for mechanistic interpretation: each simulation output, such as pressure, saturation, or the dissolved CO₂ fraction, can be broken down into contributions from capillary, diffusive, and viscous forces. This breakdown expands the interpretative value of core-flood data beyond the laboratory scale by revealing which mechanisms dominate CO₂ trapping under various petrophysical configurations (Krevor et al., 2012; Pentland et al., 2011).

Although tNavigator[®] was initially created for reservoir studies at the field scale, plug-scale challenges benefit greatly from its finite-volume architecture and fully implicit compositional solver. Numerical stability is heavily reliant on discretization and timestep controls at this resolution, where characteristic length scales are close to the representative elementary volume (REV). tNavigator[®] differs from the majority of commercial compositional simulators in that it can function with subsecond timesteps and cell volumes of 10^{-9} – 10^{-11} m³, allowing for physically meaningful modeling of capillary-dominated flow.

Lastly, scaling analysis has a stable basis thanks to this methodological framework. Any discrepancies between simulated and observed results can be directly ascribed to variations in parameterization, such as relative permeability curves or inlet boundary conditions, rather than modifications in model physics, since the numerical and experimental systems follow the same governing equations. This feature is crucial for using plug-scale simulations as calibration tools for field-scale CO₂ storage predictions.

Cylindrical geometry was defined through an ACTNUM logic mask and discretized with millimetric cells

- A domain initially fully water saturated was imposed by setting a fictitious water-gas contact above the domain
- Boundary conditions mimicking laboratory conditions were imposed through fictitious wells
- Time steps of 1 minute were employed to guarantee convergence and to record quick early saturation changes.
- The default minimal pore volume (0.000001), established to prevent division-by-zero mistakes in cells with very low porosity in order to increase numerical stability, was reduced to 10^{-12} cubic meters (keyword MINPV) according to the adopted plug scale discretization.
- The default minimal time step (0.001) established to increase numerical stability, was reduced to 10⁻¹¹ s (keyword DTMIN) according to the adopted plug scale discretization.

Different scenarios were considered accounting for homogeneous/heterogeneous spatial distribution of petrophysical characteristics and capillary curves.

The simulation setup was managed through a main DATA file written in the ECLIPSE-style syntax adopted by tNavigator[®]. The main sections of this file, which specify the simulation parameters, fluid model, grid structure, and run control, were RUNSPEC, GRID, PROPS, SOLUTION, SUMMARY, and SCHEDULE.

Management of different scenarios without re-meshing was made possible by generation of modular input files. MATLAB code was developed to write the include files.

A particular subset of data was inserted in each include file:

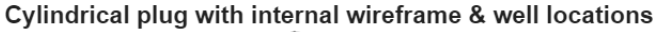
- ACTNUM.inc 3D logical array defining the cylindrical geometry by deactivating cells outside the plug radius;
- PORO.inc and PERMX.inc spatial distributions of porosity and permeability (homogeneous or heterogeneous), generated from normal distributions in MATLAB;
- WELLSPECS.inc and COMPDAT.inc definitions of injection and production wells, matching the laboratory inlet and outlet boundaries;

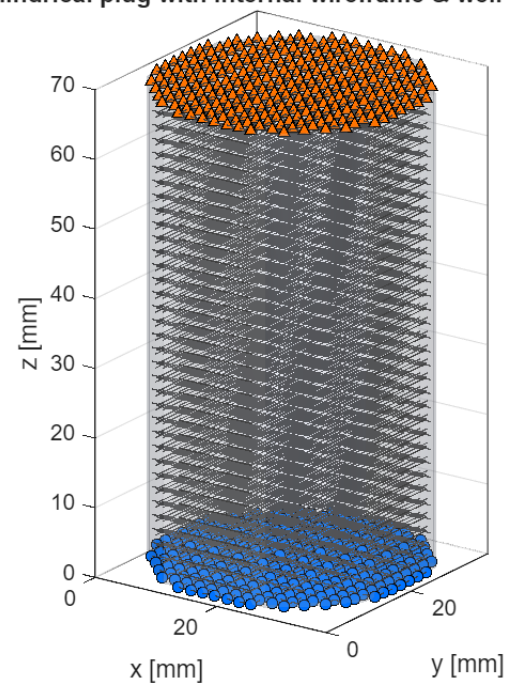
3.2 Model geometry and grid generation.

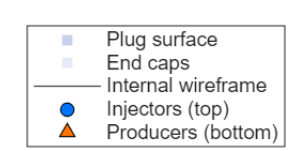
The MATLAB routines used to generate grid and property include files are provided in Appendix A.

The cylindrical plug geometry was discretized using a Cartesian grid of $76 \times 76 \times 70$ cells, with each cell having a size of 2 mm \times 2 mm, resulting in a grid that more accurately captures radial flow patterns while maintaining computational feasibility. The active cells within the cylindrical domain were defined in MATLAB via an ACTNUM mask, using a logical cylinder function applied across the full-domain Cartesian grid. While preserving computational feasibility in tNavigator[®], the grid resolution guarantees that the smallest capillary-pressure and saturation gradients are resolved.

The dimensions used in common laboratory core-flood tests (API RP40, 1998; Krevor et al., 2012) are directly reflected in the selection of a 38 mm diameter and 70 mm length. This slenderness ratio ($L/D \approx 1.8$) permits the pressure gradient to grow linearly along the flow axis while guaranteeing that end-effects are kept to a minimum. This physical proportion is maintained by the MATLAB-generated geometry, guaranteeing that each computational cell represents a physically significant subvolume of the actual plug. Direct comparison of simulated and experimental saturation profiles and pressure drop is made possible by this correspondence between the laboratory and numerical domains.







3.2.1 Cylindrical mask and ACTNUM logic

A parallelepipedal bounding box around the cylinder is defined with the physical extent of the plug's dimensions and discretized with an isotropic spacing of $\Delta x = \Delta y = \Delta z = 2$ mm

$$\circ \quad L_x = L_y = N_x \Delta x = 38;$$

$$\circ L_z = N_z \Delta z = 70. [mm]$$

$$\circ N_x = N_y = 38$$

$$O$$
 $N_z = \frac{70}{2} = 35.$

Cell centers are positioned at:

$$x_i = (i - \frac{1}{2})\Delta x;$$
 $y_i = (j - \frac{1}{2})\Delta y$

making that the geometric center $(x_c; y_c) = (L_x/2; L_y/2)$ is accurately depicted. This centering complies with tNavigator®'s finite-volume assumptions and removes systematic bias at the plug boundary.

Each cell center of the bounding box is tested against the implicit circle equation to determine the active cylindrical domain:

$$(x_i - x_c)^2 + (y_j - y_c)^2 \le R^2$$
; $R = \frac{76}{2}$ mm

Those cells that meet the inequality are tagged as active (ACTNUM = 1), all other cells are deactivated (ACTNUM = 0). The logic mask is extended in z through all axial slices ($k = 1, ..., N_z$).

A realistic cylinder with the same diameter as the actual core sample is carved out of the bounding box using this masking technique. The function write_GRDECL.m is used to export the ACTNUM array in GRDECL format to the include file ACTNUM.inc (Appendix A). To guarantee that property arrays and well completions are properly aligned within tNavigator®, flattening adheres to K-fast order (depth varying fastest) (Rock Flow Dynamics, 2024).

3.2.2 Grid resolution and physical fidelity

The 2 mm isotropic spacing that was selected offers a sufficient balance between numerical efficiency and physical fidelity. Each cell at this resolution corresponds to an 8 mm³ cubic volume, which is coarse enough to maintain the stability of the implicit solver while being fine enough to resolve the capillary heterogeneity of the plug. In CO_2 storage research, the grid aspect ratio (height / diameter ≈ 1.84) is comparable to standard experimental plugs (Pentland et al., 2011; Krevor et al., 2012). The slight approximation of a circular cross-section by a Cartesian mask introduces negligible volumetric error (< 1 %) because tNavigator® uses a finite-volume formulation on orthogonal meshes. Core-scale numerical studies where cell dimensions are at least one order of magnitude smaller than the core diameter have reported similar masked-Cartesian approaches (Oak, 1990; Blunt, 2017).

Uniform metric properties (DX = DY = DZ = 0.002 m) are inherited by every active cell. The MATLAB script ensures grid closure and removes rounding errors at the boundaries by confirming that the plug dimensions are precisely divisible by the selected cell spacing during the export process. The resulting ACTNUM, PORO, and PERMX arrays are written to distinct include files (ACTNUM.inc, PORO.inc, and PERMX.inc) for direct import into tNavigator®. They are all the same length ($38 \times 38 \times 35$).

The structural foundation for establishing boundary and flow conditions is the verified geometric configuration and cell-property assignment. The well-definition include files (WELLSPECS.inc, COMPDAT.inc) and the petrophysical maps (PORO.inc, PERMX.inc) that

regulate transmissibility and storage capacity subsequently make reference to these active-cell indices. As a result, the model geometry controls how tNavigator® interprets injection and production behavior under the dynamic controls specified in WCONINJE.inc and WCONPROD.inc, which are covered in Section 3.3, in addition to representing the physical plug.

3.3 Simulator configuration for plug-scale CO₂-brine flow: interpreting the DATA deck with CO2STORE

An ECLIPSE-style deck is used to build the plug model, which maps laboratory core-flood conditions into a finite-volume simulation and activates the compositional CO2STORE formulation. According to the tNavigator documentation's best practices and the traditional advice on reservoir-simulation input decks (Rock Flow Dynamics, 2024; Aziz & Settari, 1979), each keyword family represents a certain physical or numerical selection. (Appendix B)

RUNSPEC.

METRIC, START, and DIMENS 38 38 35 define units, reference date and the Cartesian mesh size (38×38×35 = 50 540 cells). The model is firmly in the millimetric, capillary-dominated regime that is advised for resolving steep saturation and Pc gradients at plug scale since DX/DY/DZ 50540*0.002 evenly sets the grid spacing to 2 mm (Rock Flow Dynamics, 2024). Instead of using a black-oil stand-in, the phase/physics switches WATER, GAS, and CO2STORE choose a two-phase, two-component compositional system unique to CO₂–H₂O. In order to facilitate mutual dissolution and P-T-dependent features that are managed internally by the CO2STORE thermodynamics, COMPS 2 with CNAMES 'CO2' 'H2O' expressly declares the components (Rock Flow Dynamics, 2024). The small global timestep safeguard RUNCTRL/DTMIN 1e-11 is a stabilization measure for capillary-dominated displacement with strong nonlinearity, aligning with manual recommendations to cap the minimum step when using very fine grids (Rock Flow Dynamics, 2024).

GRID

Using an activity mask INCLUDE 'ACTNUM_S1.inc', the cylinder is carved in a Cartesian box (active inside the plug, inactive outside). A constant depth datum maintains pressure initialization well-posed, while TOPS 1444*2000.0 establishes a flat datum at 2000 m TVD; gravity is insignificant at plug scale (Aziz & Settari, 1979; Rock Flow Dynamics, 2024). The vertical anisotropy MULTIPLY PERMZ 0.1, which is characteristic of consolidated sandstones and frequently used in core analogs to stop unreasonably rapid vertical leakage between layers, is copied to PERMY/PERMZ after the rock storage and transmissibility fields are assigned by PORO 50540*0.2 and PERMX 50540*100.0 (Rock Flow Dynamics, 2024). MINPV 1e-12 reduces the minimum pore volume used in flux/accumulation denominators, avoiding division by near-zero PV in thin-edge cells while preserving stability at this resolution; the manual explicitly advises tightening MINPV when moving from meter- to millimeter-scale grids (Rock Flow Dynamics, 2024).

PROPS

ROCK 1.0 1e-6, or virtually incompressible storage consistent with short plug tests, establishes the compressibility of rocks (Aziz & Settari, 1979). In order to address primary drainage at low capillary numbers, COREYWG parameterizes two-phase flow with water/gas endpoints, Corey exponents nw=3.5, ng=2.5, and a capillary-pressure flag (PC) present (Rock Flow Dynamics, 2024). Brine chemistry comes through SALINITY 0.7 (about 35–40 g/L), which CO2STORE utilizes to modify CO2 solubility and aqueous density/viscosity in the flash calculations. RTEMP 40, ZI 0, and EQUIL (below) complete the thermodynamic block, which means that the initial overall composition is pure water. This results in a fully brine-saturated reference state devoid of a free CO2 phase (Rock Flow Dynamics, 2024).

SOLUTION

Hydrostatic consistency and a fake water-gas contact are imposed above the model by EQUIL 2000 200 1500 0 0 0. In core-flood analogs, primary drainage is typically started at Sw≈1 with Pc=0 at the reference contact, with TOPS=2000 m and WOC at 1500 m (shallower than the grid) (Aziz & Settari, 1979; Rock Flow Dynamics, 2024). This matches the laboratory pre-saturation stage and prevents non-physical transients from arbitrary phase-pressure assignment.

SUMMARY

Conventional reporters (WBHP, WBP, WGIR/WGIT, FPR, FGIPG/FGIT) track the inplace/delivered gas totals, driving pressure, rates, and field pressure. In brief, capillary-controlled runs, the handbook suggests combining rate and pressure reporters to identify end-effects and constraint switching (Rock Flow Dynamics, 2024).

SCHEDULE: wells, streams, and controls.

To simulate face-injection/production and prevent erroneous "needle" injection into a single cell, wells and perforations are modularized in WELLSPECS_S1.inc and COMPDAT_S1.inc, which complete all active cells on the input and exit faces. The CO2STORE interface enforces composition-consistent injection: WINJGAS_S1.inc connects the injector to the pure-CO2 stream defined by WELLSTRE 'INJGAS' 1 0. WCONINJE_S1.inc (injector controlled by BHP or rate, depending on the file content) and WCONPROD_S1.inc (producer BHP fixed to the initial reference) are used to apply boundary conditions as mixed constraints. The suggested laboratory analogue is this inlet-pressure / outlet-BHP coupling because it eliminates ill-posed dual-pressure or dual-rate systems, pins a downstream potential, and allows for a natural rate response to capillary throttling (Rock Flow Dynamics, 2024; Aziz & Settari, 1979). The time grid TSTEP 60*0.000694444 (60 one-minute steps) is in line with manual instructions to utilize short steps early on in order to sustain Newton convergence under steep Pc gradients and record quick saturation transients (Rock Flow Dynamics, 2024).

3.4 WCONINJE.inc and WCONPROD.inc – dynamic control of well constraints (constant ΔP CO₂ injection); Petrophysical properties and fluid system definition

The inlet and outlet boundaries are enforced via well controls to mirror laboratory manifolds while ensuring robust convergence in the fully implicit solver. At the inlet, injectors are constrained by constant pressure using WCONINJE (CO₂ stream), at the outlet, producers are constrained by constant bottomhole pressure using WCONPROD, which fixes the sink pressure to the initial reference (Honarpour et al., 1986; Oak, 1990; Aziz & Settari, 1979). The CO₂ composition of the injected stream is defined with WINJGAS, set to $y_{CO_2} = 1.0$, $y_{H_2O} = 0.0$, consistent with laboratory gas injection into a fully brine-saturated plug (Rock Flow Dynamics, 2024).

The ability of the rock matrix to transfer and store fluids is how petrophysical description characterizes it. Porosity and permeability are the two primary factors that control these properties.

Porosity (φ)

The percentage of a rock's pore volume that can hold fluids is known as porosity. The modeled plug's mean porosity, which was 0.20 with a standard variation of \pm 0.02, was in line with values for fine sandstones that are frequently employed in lab tests (Bachu, S., 2008).

Permeability (k)

The rock's permeability regulates its capacity to transfer liquids. The chosen mean permeability was 100 mD (σ = 10 mD). One-tenth of horizontal permeability (PERMZ = 0.1 * PERMX) was chosen as the vertical permeability for anisotropy. Consolidated sandstones utilized in CO₂-brine displacement tests typically have values like this (Krevor et al., 2012).

Rock compressibility

The ability of the rock matrix to reduce its pore volume in response to an increase in pressure is known as rock compressibility. It is often expressed in bar⁻¹ or Pa⁻¹ and is defined as the fractional change in pore volume per unit change in pressure. The rock compressibility in this investigation was fixed at 1*10⁻⁶ bar⁻¹, which is equivalent to practically incompressible circumstances that are typical of laboratory tests with little pressure changes. Since pore volume changes are minimal in such conditions, it is reasonable to assume that fluid compressibility and saturation dynamics, rather than solid framework deformation, govern storage variations.

Phases and components

Two miscible components make up the fluid system employed in this study: carbon dioxide (CO₂) and water (H₂O). These components can coexist in two thermodynamic phases: an aqueous brine phase and a gaseous CO₂-rich phase. The physical conditions seen in saline aquifers, where injected CO₂ reacts with formation water are replicated in this setup.

The portion of the injected CO₂ dissolves into the aqueous phase, whereas water can evaporate into the gas phase, allowing the CO2STORE formulation to simulate the mutual solubility of CO₂ and water. The primary trapping mechanisms in geological storage, especially solubility trapping, which improves long-term CO₂ containment, must be represented by this relationship.

Salinity and temperature

The brine salinity, which is typical of laboratory settings for saline aquifer analogs, was fixed at 0.7 mol/kg, or around 35-40 g/L NaCl. The experimental conditions in which CO₂ is gaseous or near-critical were represented by the reservoir temperature, which was defined as 42 °C.

Units and pore-volume rationale

The cylinder volume for a plug with dimensions of 38 mm in diameter and 70 mm in length is:

$$V_{plug} = \pi r^2 h = \pi (0.019)^2 \cdot 0.07 \approx 7.94 \cdot 10^{-5} \text{ m}^3$$

so for $\phi = 0.20$ the pore volume is:

$$PV = \phi \cdot V_{plug} \approx 1.59 \cdot 10^{-5} \text{ m}^3$$

The outlet BHP in WCONPROD is fixed to the initial pressure, ensuring a consistent reference sink while the inlet maintains the laboratory-specified volumetric drive (Aziz & Settari, 1979; Rock Flow Dynamics, 2024).

Relative permeability and capillary pressure

Corey-type correlations (COREYWG) for gas and water relative permeabilities were used to define multiphase behavior: exponents were changed to correspond to standard displacement curves found in laboratories. In order to guarantee realistic transition zones between the gas and water phases, capillary pressure functions (PCGW) were established.

The integrated rock and fluid characterization enables realistic simulation of two-phase flow under laboratory settings and constitutes the basis for assessing the sensitivity of CO₂ displacement to heterogeneity, boundary conditions, and capillary behavior.

The same active-cell indices that are used in WELLSPECS/COMPDAT and the property maps (PORO, PERMX) are referred to by all well controls (WCONINJE, WCONPROD, and WINJGAS). Deck checks verified that the cumulative injected volume (from WCONINJE) matched the target pore-volumes injected and that the relative material-balance error stayed within an acceptable tolerance for plug-scale runs. Arrays were exported in K-fast to preserve spatial alignment between completions and cell properties (Rock Flow Dynamics, 2024; Aziz & Settari, 1979). In order to make sure that the intended cross-sections are affected by rate/BHP limitations and that transmissibilities represent the anticipated heterogeneity, this verification step is essential.

3.5 Inlet-outlet boundary conditions

The code designates active cells on the first and last axial slices (k = 1 and $k = N_z$) as inlet and outlet faces, respectively. In order to force tNavigator to replicate laboratory boundary conditions, fictitious wells were generated covering these circular cross-sections. Well placement and completions across active inlet/outlet cells were printed on WELLSPECS.inc and COMPDAT.inc include files in ECLIPSE-style.

At the inlet, fictitious injectors were assigned a constant pressure (WCONINJE keyword) with a gas stream composition of 100% CO₂ specified by WELLSTRE and WINJGAS include files. This configuration replicates the experimental state in which a steady volumetric flow of CO₂ enters the plug's upper surface.

To simulate a constant-pressure outlet where displaced brine can freely flow, fictitious producers were defined at the outlet with fixed bottom-hole pressure (WCONPROD keyword) equal to the initial reservoir pressure (200 bar).

In the formulation that tNavigator® uses, the rate–pressure combination used here guarantees unconditional numerical stability. The solver prevents singular matrices that would arise if both ends were pressure-controlled or both rate-controlled when the injection well is confined by rate (WCONINJE) and the producer by bottom-hole pressure (WCONPROD) (Aziz & Settari, 1979). Total-mass balancing closure is made possible at each time step by the fixed-pressure outlet providing a reference potential and the constant-pressure inlet. It has been shown that these mixed Dirichlet–Neumann boundary conditions minimize numerical oscillations close to the outflow and best replicate core-flood experiments (Honarpour et al., 1986; Lie, 2019).

These controls guarantee that the pressure-controlled injection at the inlet and pressure-controlled discharge at the outlet, which are the driving forces seen in the lab, are replicated in the numerical model.

The WINJGAS.inc file defines the gas stream composition associated with the injection wells, in this case a pure CO₂ stream (mole fraction 1.0 for CO₂ and 0.0 for H₂O), as required by the CO2STORE module. This definition ensures that the injected phase corresponds exactly to a single-component CO₂ gas, consistent with laboratory injection conditions.

To verify that flow lines stayed parallel to the plug axis and that there was no lateral leakage through deactivated cells, pressure maps and velocity-vector plots were exported from tNavigator® during model verification. This diagnostic made sure that numerical end-effects were successfully removed and that the boundary conditions replicated a one-dimensional displacement regime common in core-flood studies (Oak, 1990; Blunt, 2017).

3.6 Initialization

Prior to the start of CO₂ injection, the model initialization block specifies the system's initial thermodynamic and saturation conditions. Initialization was set up in order to replicate controlled laboratory CO₂-brine displacement tests.

To make sure that no free CO₂ existed prior to the first time step, the initialization routine in tNavigator® was run in single-phase mode during model setup. In order to verify total hydrostatic consistency, the simulator internally solves the pressure field until the residual of the mass-balance equations drops below 10⁻⁸. The SCHEDULE portion doesn't turn on the CO₂ injection wells until this convergence is reached (Rock Flow Dynamics, 2024).

Before injection, it was assumed that the plug was completely saturated with brine, which is equivalent to the pre-conditioning phase in laboratory experiments, where the sample is vacuum-saturated. The major drainage condition characteristic of laboratory core floods is replicated by achieving 100% brine saturation before CO_2 injection (Krevor et al., 2012). With P_c =0 at the reference contact, the application of the EQUIL keyword guarantees that initial phase pressures fulfill the static capillary equilibrium relation throughout the plug. By using this initialization, non-physical transients that might arise from assigning phase pressures at time = 0 randomly are avoided (Aziz & Settari, 1979). Assuming equilibrium prior to injection is physically reasonable and avoids misleading saturation oscillations during the first time step since capillary forces predominate at the plug scale ($N_c = 10^{-6}$).

In order to replicate the laboratory setting where CO₂ exists in a gaseous or near-critical state, the initial pressure and temperature were set at 5 bar and 42 °C respectively. A consistent reference pressure of 200 bar is established across the plug by the EQUIL keyword. Hydrostatic pressure gradients are minimal since the simulated domain is a small cylindrical core. Gravity effects were turned off to prevent fictitious vertical pressure changes, keeping the sample's pressure constant.

Diagnostic maps were exported from tNavigator® following the completion of the initialization procedure to confirm the single-phase pressure distribution and uniform brine saturation ($S_w = 1.0$). The Initialization Report verified that all active cells had the same water pressure and 0% gas saturation, proving that the equilibrium contact and pressure assignments were applied appropriately. By ensuring that the simulation begins with a single-phase, fully equilibrated reference state, this validation made it possible to trace any subsequent CO_2 invasion to imposed boundary conditions rather than initialization artifacts (Lie, 2019; Rock Flow Dynamics, 2024).

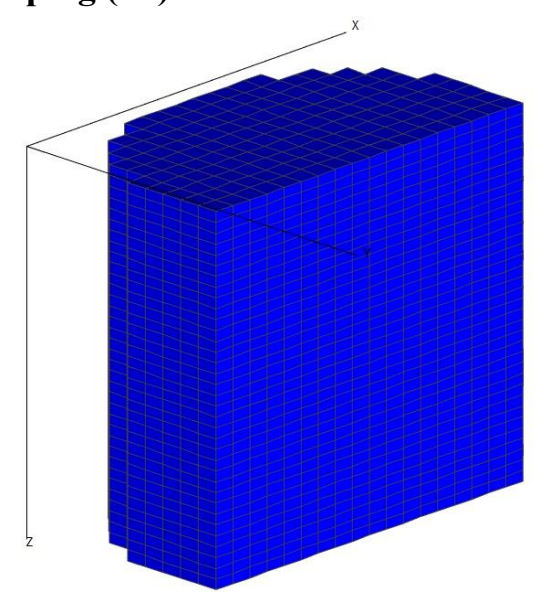
All of above ensures that the system is thoroughly saturated with brine, starts at a constant temperature and pressure, and is physically compatible with laboratory settings. The progression of CO₂ saturation, pressure buildup, and trapping behavior can be precisely examined from this start since it offers a reliable and repeatable reference condition.

3.7 Simulation scenarios

To evaluate the impact of spatial heterogeneity of porosity and permeability on CO₂ displacement in a cylindrical plug, four simulation scenarios were established. The internal distribution of rock properties is the only difference between the cases, which were all conducted under the same thermodynamic and flow conditions. The process enables a methodical assessment of how pore-scale structure affects the spatial distribution of trapped CO₂, water displacement efficiency, and saturation fronts (Blunt, 2017; Bear, 1972).

3.7.1 Homogeneous plug (S1).



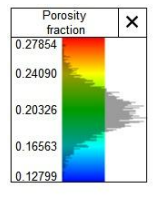


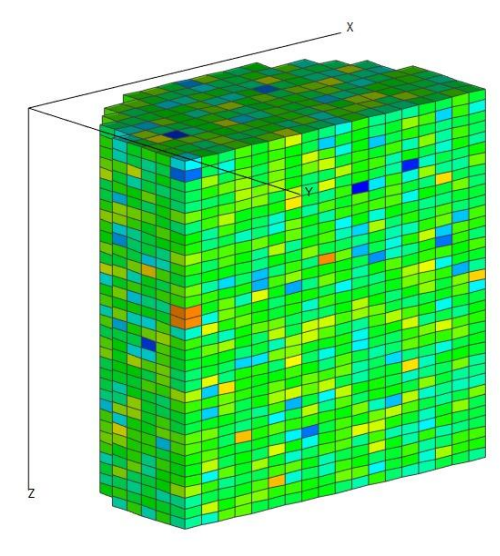
The reference configuration is the first example. When porosity and permeability are assigned uniform values across all active cells, the porous medium is said to be fully homogeneous:

- $\phi = 0.20$ is the porosity.
- Permeability: 100 mD = k

This configuration offers a baseline against heterogeneous cases and is the numerical counterpart of a perfectly isotropic core sample (Dullien, 2012). Internal barriers and preferential high-permeability streaks are absent, allowing the CO₂ front to move symmetrically and smoothly downward from the injector face. The displacement behavior linked exclusively to the imposed pressure gradient and fluid properties can be isolated because saturation gradients and pressure profiles are uniform (Lake, 1989).

3.7.2 Random porosity – uniform permeability (S2).

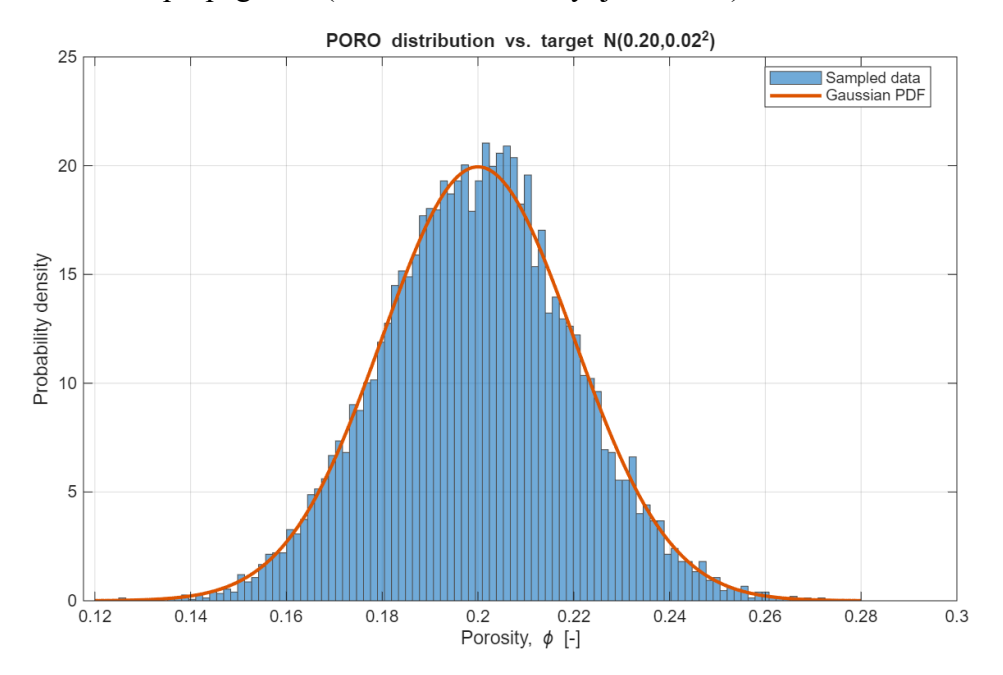




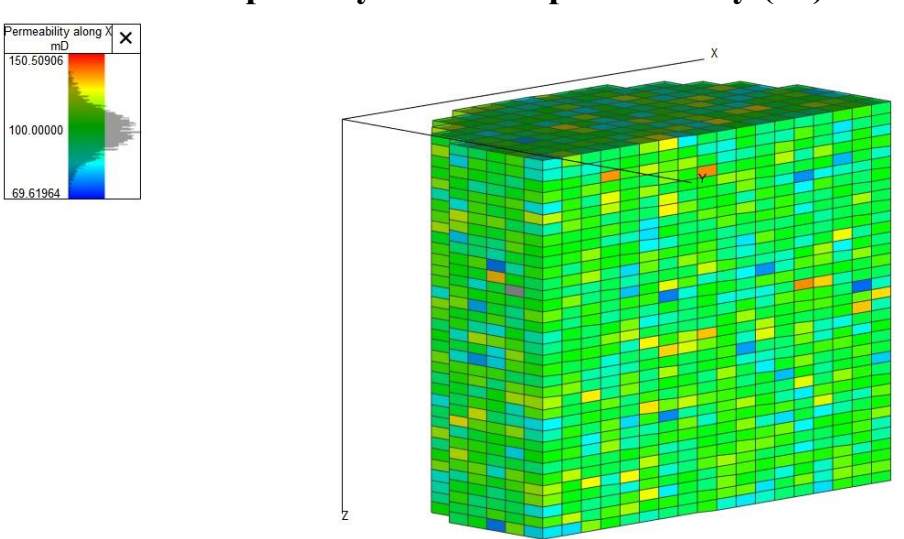
Permeability is maintained at 100 mD in this configuration, but porosity values change spatially in response to a randomly distributed, normally distributed field:

- At $\phi = 0.20 \pm 0.02$, porosity
- Permeability: constant, k = 100 mD

MATLAB was used to create the porosity field, which was then limited to active cylindrical cells and sent to tNavigator via INC files. In this instance, uniform hydraulic conductivity is maintained while only the impact of pore volume heterogeneity is isolated. Saturation distributions and storage capacity are affected by changes in local pore volume, but the uniform permeability field still largely controls the CO₂ front's propagation (Bourbiaux & Kalaydjian, 1990).



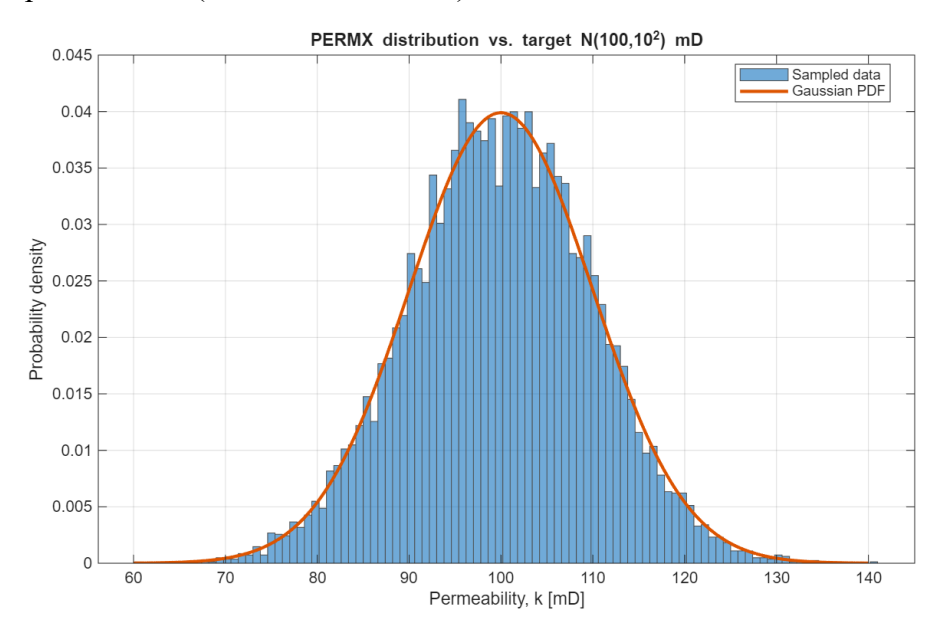
3.7.3 Uniform porosity – random permeability (S3).



In the third case, homogeneous porosity is preserved while permeability heterogeneity is introduced. With a standard deviation of 10 mD and a center of 100 mD, permeability values follow a normal distribution:

Porosity: constant φ = 0.20
Permeability: 100 ± 10 mD = k

This case allows the evaluation of channeling and preferential flow paths caused by changes in hydraulic conductivity (Oeyen & Van der Zee, 2005). CO₂ is predicted to migrate more quickly through high-permeability streaks, even though the total pore volume stays constant throughout the domain. This would cause the displacement front to advance unevenly and cause an earlier breakthrough in specific areas (Kaviani et al., 2018).



3.7.4 Random porosity and random permeability (S4)

Both property variations are combined into a single heterogeneous configuration in the final scenario. Gaussian sampling is used to independently assign porosity and permeability:

• At $\phi = 0.20 \pm 0.02$, porosity

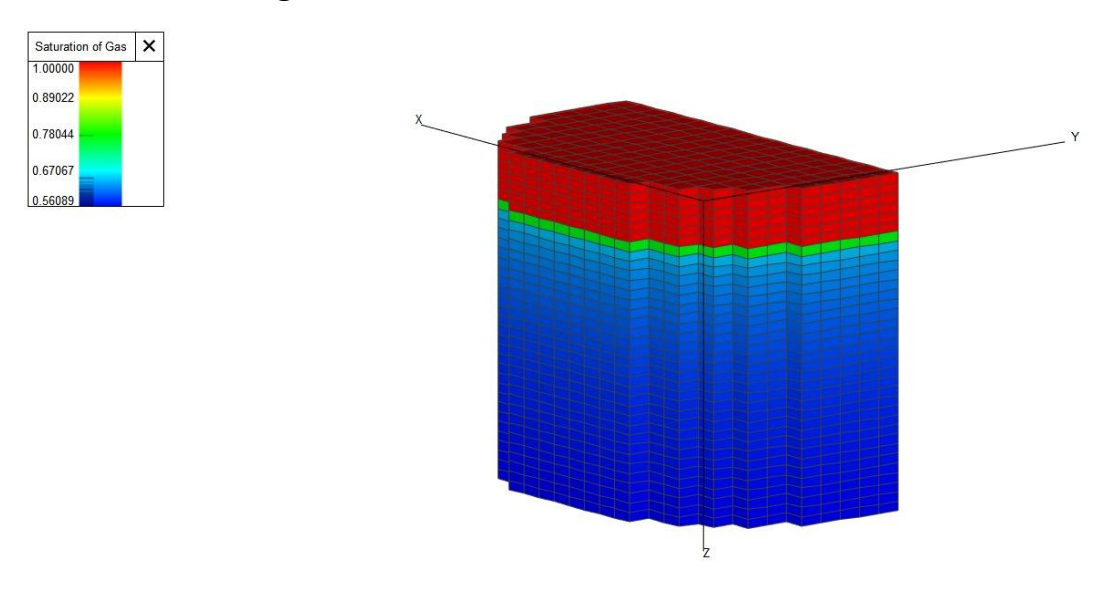
• Permeability: $100 \pm 10 \text{ mD} = \text{k}$

In this instance, spatial variations in both hydraulic and pore volume properties coexist, making it the closest numerical analog of a real core sample (Deutsch & Journel, 1998). Complex CO₂ displacement patterns, such as bypassing, early breakthrough, and differential residual trapping, can result from the interaction of locally varying pore volume and conductivity (Zhou et al., 2014).

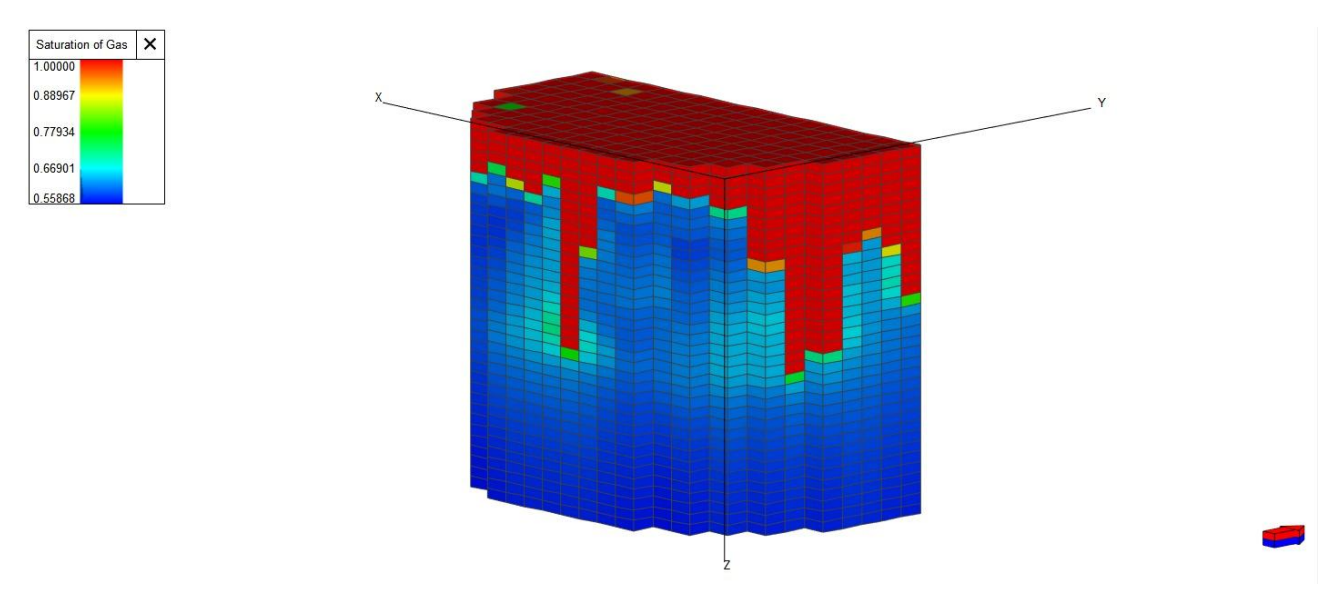
4 Results and discussion

4.1 Propagation of gas for each scenario at the same time step (100 min)

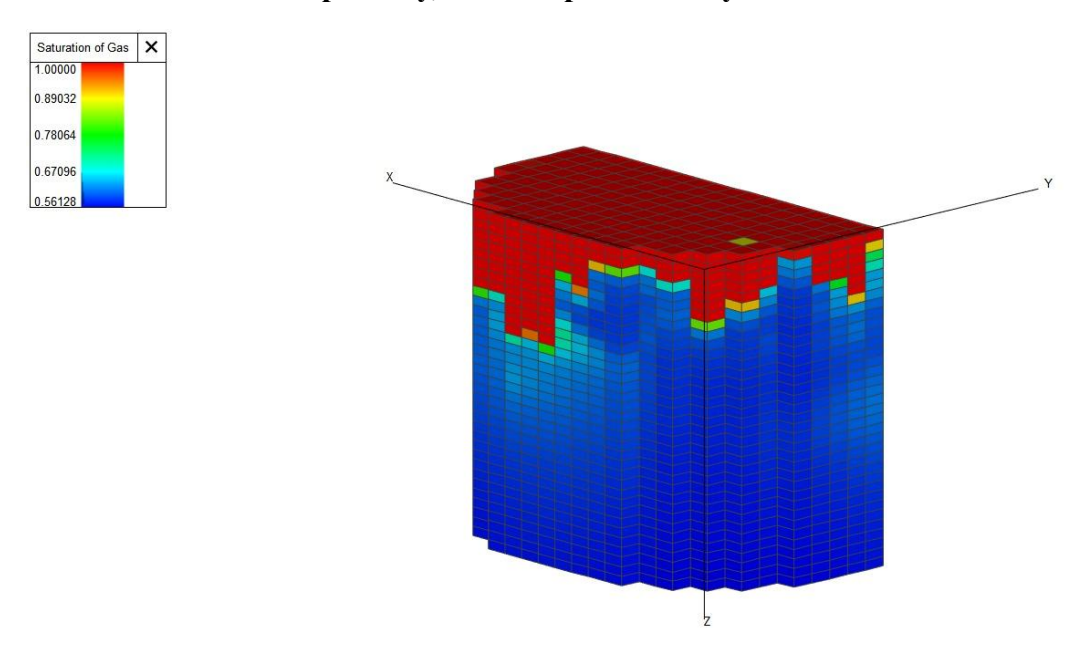
Scenario 1 – homogeneous case:



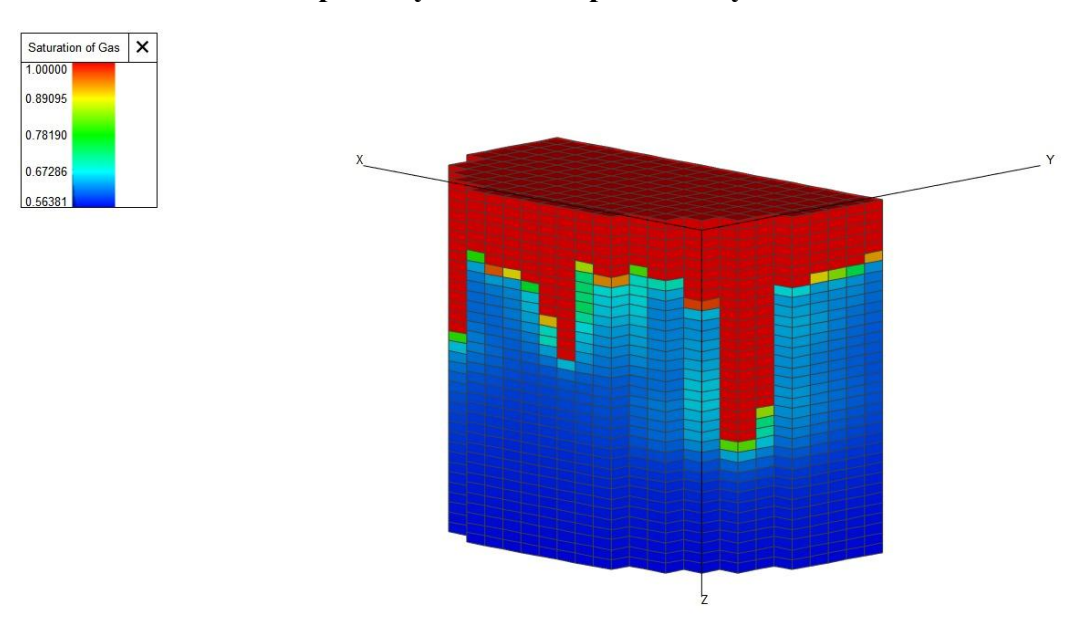
Scenario 2 – Random porosity, uniform permeability



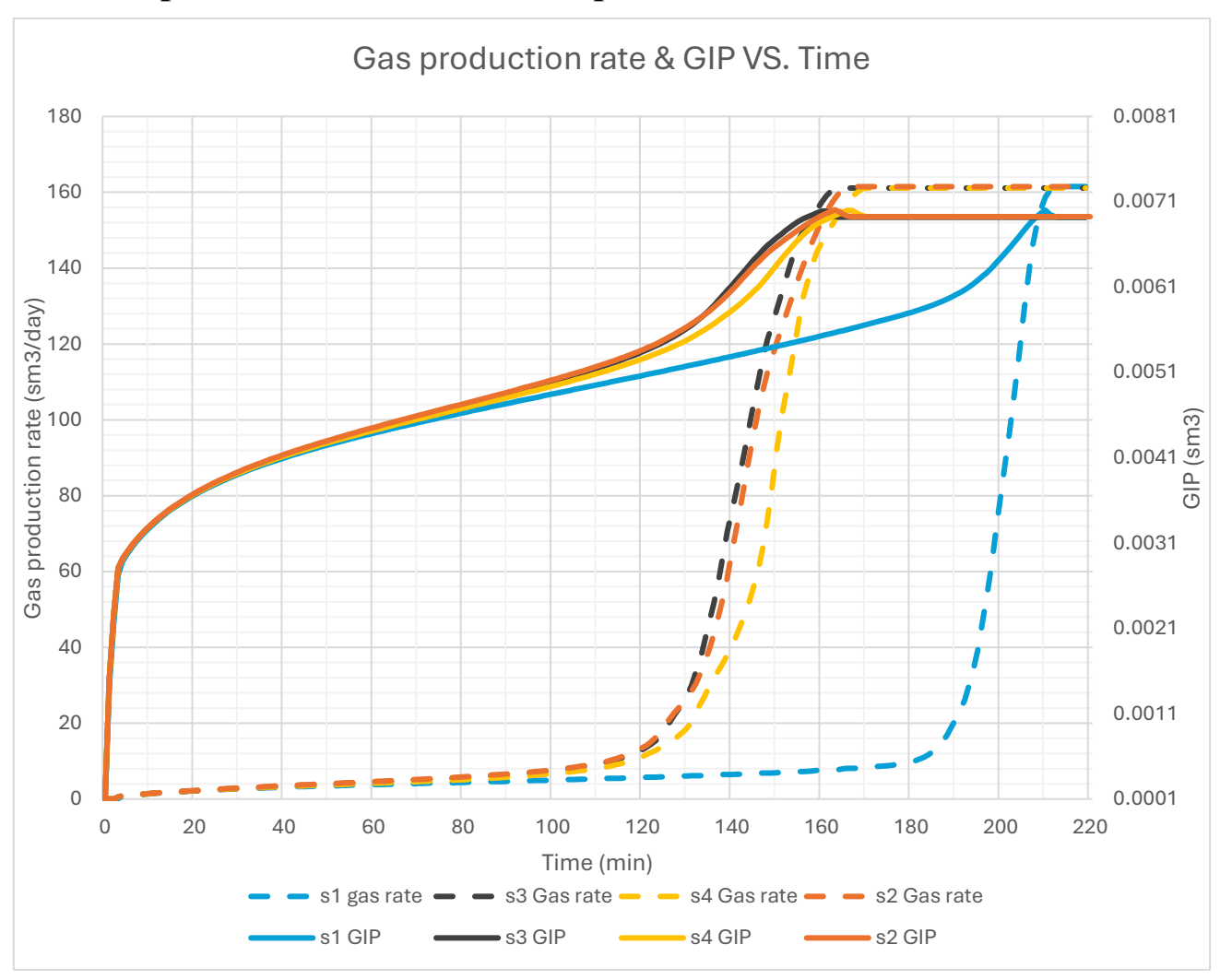
Scenario 3 – uniform porosity, random permeability:



Scenario 4 – Random porosity & random permebility:



4.2 Gas production rate & Gas in place evolution vs. Time



All of the scenarios show a sharp rise in gas production rate after breakthrough, although the models' start and production ramp steepness vary greatly. At around 200 minutes, breakthrough takes place in the homogenous Base Case (S1), following which the output rate increases dramatically and settles around 160 sm³/day. Under completely homogenous conditions, this behavior indicates a consistently distributed pore volume and a predicted displacement front.

The breakthrough is significantly earlier when porosity heterogeneity (S2) is introduced; it happens around 50 minutes earlier than in S1. Additionally, the rate increase that follows is steeper and arrives at the post-breakthrough plateau sooner. Low-porosity zones, which decrease local storage capacity and encourage earlier CO₂ saturation and quicker displacement of brine along favored pathways, are thought to be the cause of this acceleration. The redistribution of pore volume changes the system's compressibility and the pressure-saturation response, even while permeability stays constant in both situations. This illustrates how breakthrough timing and dynamic injectivity can be significantly impacted by porosity heterogeneity alone, regardless of transmissibility.

The gas production ramp sharpens and the breakthrough switches much earlier than in S2 when permeability heterogeneity (S3) is introduced. Low-permeability areas hold water for longer and make a small contribution to early-time transport, whereas high-permeability streaks produce preferential flow channels that speed up frontal progress. Instead of just storage, this behavior illustrates the traditional sensitivity of multiphase displacement to spatial differences in conductivity.

Out of all the situations, the combined heterogeneity example (S4) yields the fastest breakthrough since both porosity and permeability vary regionally. Improved flow transmissibility and decreased pore volume work together to accelerate saturation build-up and early well-to-well pressure transmission. This model shows the greatest increase in gas production, demonstrating that displacement non-uniformity is amplified by simultaneous heterogeneity in flow and storage parameters.

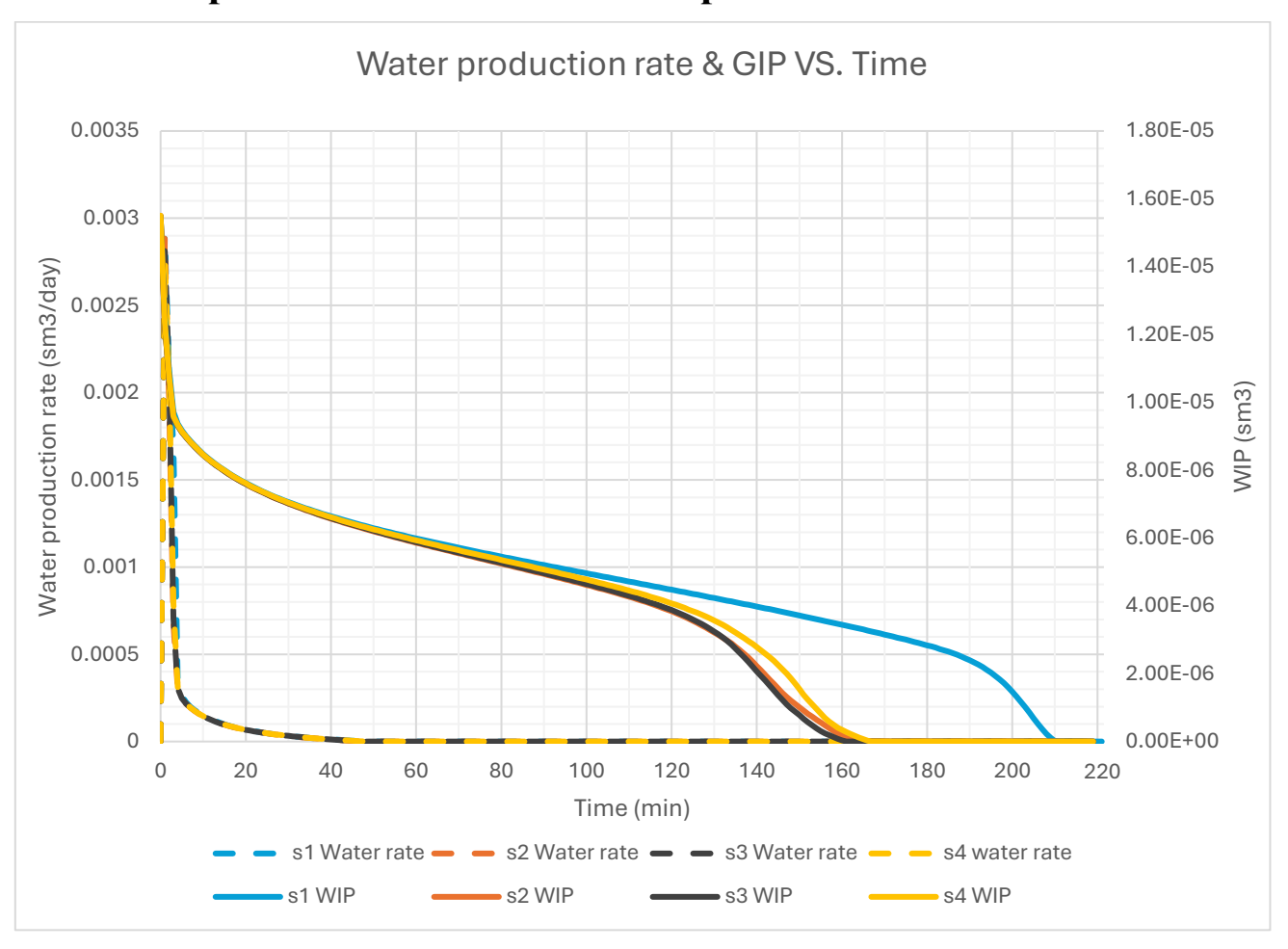
The growth of gas in place (GIP) follows a similar qualitative trend in all four simulations, reflecting the progressive drainage of brine and the gradual filling of the pore space by CO₂. The curves for all scenarios are almost identical during the first 30 minutes of injection, indicating that the early displacement acts as a piston-like front that has not yet been affected by spatial changes in rock qualities.

After this initial phase, variations occur based on whether the plug is homogenous or heterogeneous. Due to the radially symmetric invasion of gas into the medium without access to preferential flow or storage zones, the homogeneous reference scenario (S1) shows the slowest and most consistent increase in GIP. In contrast, after about 100 minutes, all of the heterogeneous cases (S2, S3, and S4) show a rapid accumulation of gas, reaching greater GIP values much earlier than S1.

The random-porosity case's GIP curve flattens after the breakthrough transition, indicating an earlier connection between the injector and producer as a result of quicker local drainage pathways. In the meantime, the homogeneous case keeps increasing more gradually, proving that while porosity variability shortens the storage phase prior to breakthrough, it speeds up CO₂ invasion.

It is evident that uniform rock qualities delay breakthrough not because of lower final storage but rather because the invasion happens more uniformly and hence more slowly. The homogeneous area continues to gather gas gradually and only approaches the same GIP values at a much later time.

4.3 Water production rate & Water in place evolution vs. Time



The water production rate exhibits the same distinctive pattern in all four cases: a steep drop just after injection begins, followed by a slow decline toward zero. This demonstrates that the entrance of the CO₂ front, which effectively displaces the mobile brine phase, is the primary control on early-time water removal. In every model, the water rate decreases by over two orders of magnitude in the first five to six minutes, suggesting that the majority of the producible water is released in a little period of time.

In contrast to the heterogeneous models, the homogeneous case (S1) shows a somewhat slower drop in water rate, even if the general behavior is the same across scenarios. This discrepancy results from the displacement front advancing more uniformly when there are no spatial variations in pore volume or flow capacity. On the other hand, the early phases of the heterogeneous cases retain slightly more mobile water, which is indicative of the impact of different pore storage and flow paths. However, as the system shifts to a gas-dominated flow regime, all curves converge to the same near-zero water rate.

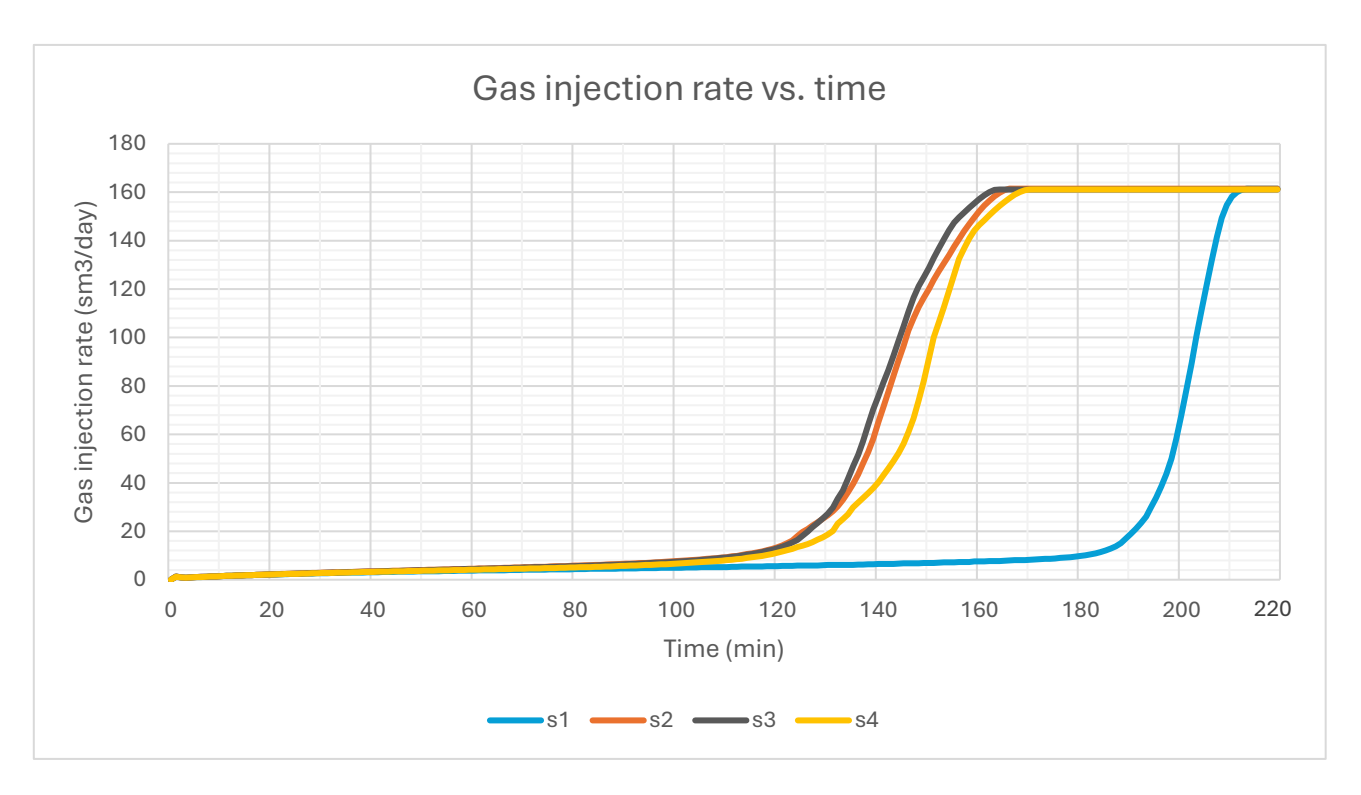
As CO₂ infiltrates the medium, brine is gradually removed from the pore space, as evidenced by the decrease in water in place (WIP). All four scenarios show almost the same behavior in the early stages of injection (0–40 minutes), indicating that spatial changes in rock characteristics have not yet

impacted the initial displacement front. Regardless of the porosity or permeability structure, the water phase remains continuous during this phase, and drainage moves forward like a piston.

Once the displacement front starts interacting with the plug's internal variability, differences start to appear. After about 100 minutes, the homogeneous example (S1) shows the fastest drop in water content, suggesting that the gas front moves evenly and effectively through the medium, creating a dramatic change from brine-filled to gas-dominated circumstances. Without heterogeneity, there are no areas where pore volume or capillary entry pressure can prevent total drainage, leading to almost nil water content soon after breakthrough.

On the other hand, throughout the same time period, all of the heterogeneous examples (S2, S3, and S4) retain greater amounts of water. The porosity-only example (S2) exhibits the slowest WIP decrease, and even after breakthrough, a sizable residual brine volume remains. This is due to the fact that low-porosity areas serve as local storage pockets with higher capillary entry pressure and delayed CO₂ invasion. The overall trend is similar when permeability is heterogeneous (S3), but the shift is marginally more abrupt than in S2, indicating that variability impacts flow transmissibility rather than storage capacity. Between S2 and S3, the combined heterogeneity case (S4) drains more effectively than the porosity-only case while holding onto more water than the homogeneous baseline.

4.4 Gas injection rate Vs. Time



The same upper injection limit of about 160 sm³/day is eventually reached by all four simulations, indicating that permeability is the primary determinant of long-term injectivity. This value is the maximum deliverability permitted under the imposed bottom-hole pressure (BHP)

constraint of 220 bar. This transient behavior illustrates how pore-scale heterogeneity influences the resistance to CO₂ invasion during the early phases of displacement, as the time needed to attain this plateau varies greatly between the situations.

With a delayed acceleration phase and a rate plateau onset after about 210 minutes, the homogeneous reference example (S1) exhibits the slowest injectivity development. Because there are no favored channels, the pressure builds up more smoothly and gradually before the BHP limit is reached because CO₂ must displace brine equally.

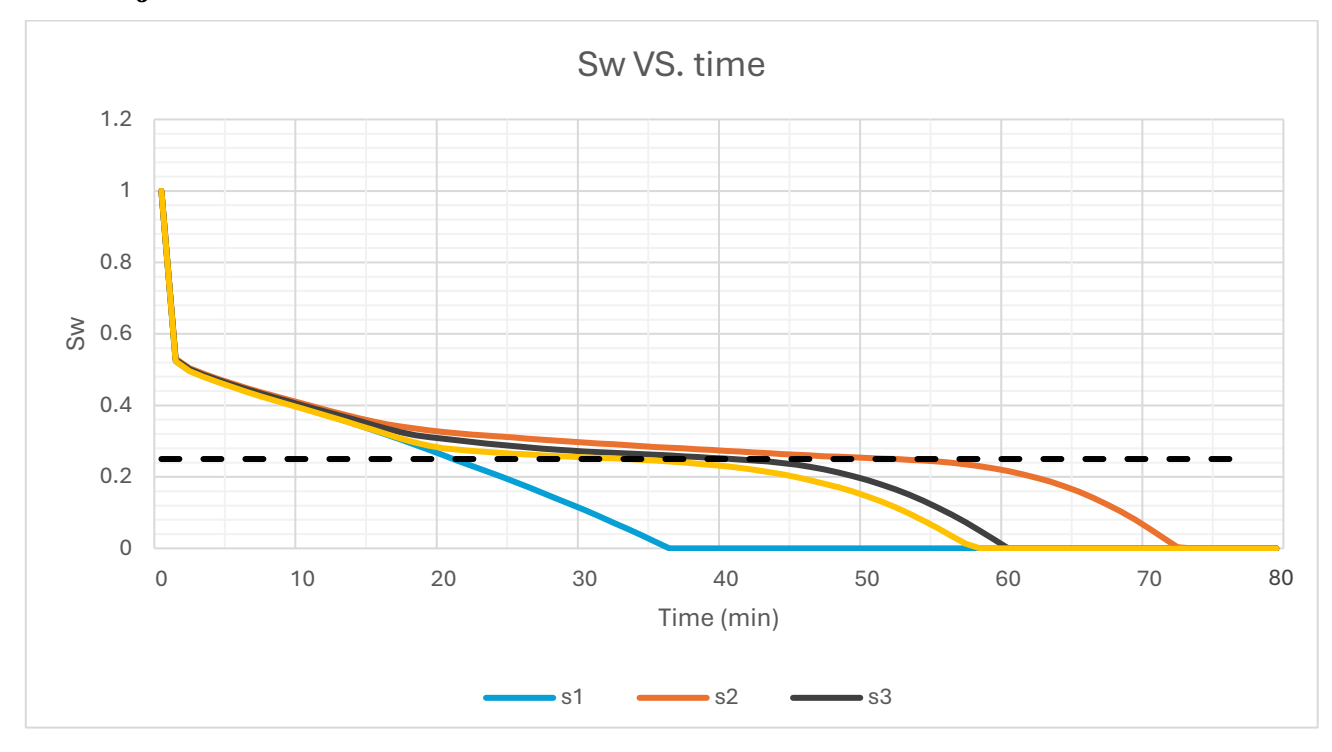
The three heterogeneous examples (S2, S3, and S4), on the other hand, show a significantly earlier transition to high injection rates, stabilizing about 40–60 minutes earlier than S1. The three curves converge closely despite their various sources of heterogeneity, suggesting that both permeability and porosity variability lower the system's effective flow resistance in comparison to the perfectly uniform case.

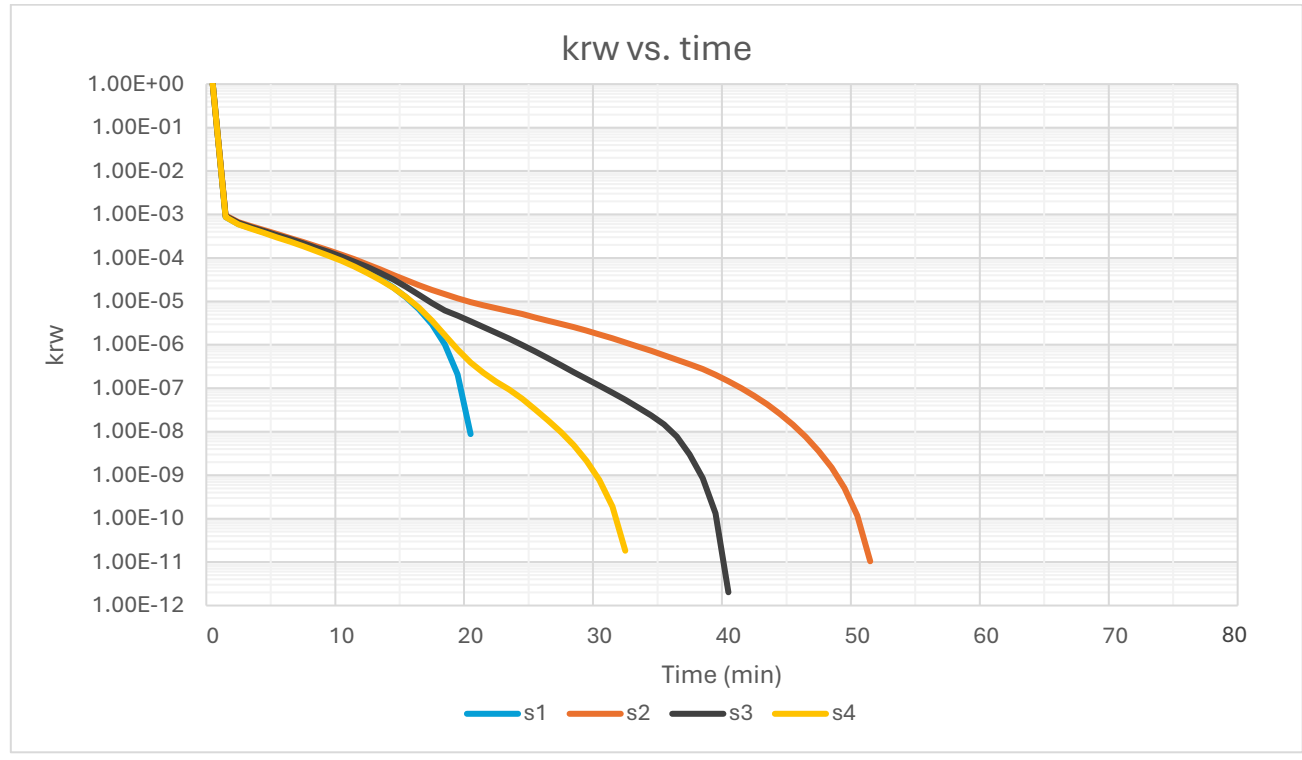
It is confirmed that spatial variability in pore volume alone is sufficient to create regions in which the gas saturation rises rapidly, allowing for earlier communication between the injector and the production boundary. The scenario with random porosity but uniform permeability (S2) accelerates injection earlier than S1. This confirms the well-documented mechanism whereby CO₂ lowers the necessary capillary entry pressure in larger, better-connected pores by invading them first.

The reaction is similarly amplified when the heterogeneity operates on permeability (S3) instead. Here, the existence of high-permeability streaks that locally boost transmissibility and thereby decrease viscous pressure losses is responsible for the shorter breakthrough time rather than changes in storage capacity. The similarity between S2 and S3 implies that either form of heterogeneity — pore volume or flow conductivity — can shorten the transient phase.

When both the permeability and porosity fields are spatially variable, the combined-heterogeneity example (S4) results in the earliest and sharpest increase in injection rate, demonstrating an additive effect. The system reaches the BHP limit in the shortest amount of time in this arrangement because the gas front encounters locally reduced water saturation more quickly in addition to preferring moving down high-transmissibility paths. As a result, out of all the situations, S4 represents the displacement environment with the least resistance.

4.5 Drying-out behavior and loss of water mobility during CO₂ injection





The development of water saturation (S_w) and relative permeability to water (k_{rw}) in each of the four simulated scenarios validates the start of a typical drying-out process close to the injection face during CO_2 flooding. By gradually dislodging the associated aqueous phase, the injected gas lowers

water saturation below the critical threshold, which is the point at which water stops acting as a mobile phase. The rate at which desaturation takes place varies based on the geographical distribution of petrophysical parameters, even though the overall trend is constant across all cases.

After around 35 minutes of injection, the homogeneous base scenario (S1) experiences a quick and monotonic fall in S_w, which results in the total loss of mobile water. This illustrates how a uniform drainage front can move through the pore network since internal capillary barriers are absent. The heterogeneous situations (S2–S4), on the other hand, show a slower decrease in saturation and longer-lasting residual water. While low-porosity zones that retain brine through capillary trapping delay desaturation in the random-porosity case (S2), spatial variations in both pore volume and transmissibility result in a more gradual transition from water-wet to gasdominated conditions in the random-permeability (S3) and combined heterogeneity (S4) cases. The persistence of elevated S_w in these cases demonstrates that heterogeneity inhibits uniform displacement and promotes the formation of disconnected water clusters that remain trapped even under continuous gas injection.

The saturation tendencies are reflected in the equivalent decrease in $k_{\rm rw}$. As $S_{\rm w}$ gets closer to the irreducible level, $k_{\rm rw}$ falls toward zero in all cases, signifying the loss of hydraulic continuity in the aqueous phase. The point at which $k_{\rm rw}$ becomes insignificant varies, though; in S1, the decrease happens sooner and more suddenly, while in S2–S4, residual water is sporadically connected for a longer period of time, maintaining non-zero (but fast declining) $k_{\rm rw}$ values before finally disappearing. This behavior demonstrates that variations in permeability and porosity have a considerable impact on the kinetics of water-phase immobilization but do not substantially change the outcome of desaturation.

One important finding in all four cases is that, despite reaching the nominal irreducible water saturation that the relative permeability curves predicted, water saturation keeps declining. Advective transport and phase exchange with the flowing CO₂ stream not only immobilizes disconnected water ganglia and thin corner films, but also gradually removes them, confirming the existence of a real drying-out mechanism. These isolated water clusters are periodically mobilized and carried away as micro-droplets or vapour-phase water as the gas front advances, causing S_w to drop below the tabulated irreducible value. This behavior is not reproducible by drainage models that are just capillary-driven.

Once this extra water removal starts, viscous coupling and film-flow resistance at the pore walls are eliminated due to the absence of wetting phase films, which causes a dramatic rise in relative permeability to gas. The change from capillary-controlled two-phase flow to single-phase gas flow with residual, unconnected brine is indicated by the sharp drop in k_{rw} and the abrupt acceleration in gas mobility. Drying-out close to the injector occurs before salt precipitation and injectivity loss, but it is nonetheless detectable even without salt (i.e., as a purely hydrodynamic desaturation stage). As a result, the simulations replicate not only primary drainage but also the physical conditions that exist in the early stages before evaporative brine loss and salt blockage, which are shown in laboratory experiments.

5 Conclusion

In order to replicate laboratory core-flood conditions and elucidate the function of pore-scale mechanisms in early-time displacement and trapping, this thesis offered a thorough computational study of the dynamics of CO₂ injection into a fully brine-saturated cylindrical rock plug. The study has been carried out adopting the compositional CO2STORE option in tNavigator® and creating a MATLAB-based methodology to generate and populate the 3D cylindrical grid.

Four different scenarios were considered: Homogeneous porosity and permeability (S1), homogeneous permeability with random porosity distribution (S2), Homogeneous porosity with random permeability distribution (S3), and heterogeneity in both porosity and permeability (S4). The considered scenarios provide a first analysis of the effects of permeability-controlled transmissibility and porosity-controlled storage capacity on CO₂ - water displacement.

The simulations replicated basic characteristics of laboratory-scale drainage into water-wet porous medium in all scenarios, as has been extensively documented in the literature. In each instance, the breakthrough behavior was seen, which is defined by a increase in the rate of gas production and a commensurate decrease in the rate of water production. However, the enforced heterogeneity had a significant impact on the time and slope of these changes. Random permeability (S3) enhanced this effect by permitting faster flow via high-transmissibility conduits, but random porosity (S2) induced an earlier gas breakthrough because of reduced local pore volumes along favored paths. The fastest breakthrough and the most uneven sweep were observed in the combined heterogeneity scenario (S4), demonstrating that flow symmetry is considerably distorted by combined changes in φ–k fields.

These patterns were supported by storage dynamics as assessed by gas-in-place and water-in-place curves. The homogeneous instance showed a more gradual post-breakthrough stabilization and a uniform transition from the brine-saturated to the gas-invaded condition, which is compatible with piston-like displacement. However, the GIP and WIP curves diverged earlier and had a steeper starting slope in situations with random porosity or permeability, suggesting earlier injector—producer connection and faster local desaturation. All scenarios converged to comparable late-time values for cumulative gas retention and gas production rates, indicating that heterogeneity only determines the direction and speed of fluid invasion while permeability and fluid properties largely control the overall storage capacity.

The adoption if the CO2STORE option provided a representation of the drying-out effect. Water saturation first decreases as the injected CO₂ enters a fully brine-saturated medium because mobile brine is displaced. This reduction persists even after the critical water saturation ($S_{wc} = 0.25$) is reached, at which point water relative permeability has already reached zero. Since the aqueous phase is stationary at that point, evaporation and diffusion of water into the CO₂ stream—which eliminates liquid water mass by vaporization—cause this additional reduction instead of displacement. As a result, a progressive transition from immobile residual brine to completely dry conditions ($S_w \rightarrow 0$) at the inlet in the considered scenarios. This work is therefore dedicated to the analysis of possibility of simulating plug experiments using a conventional reservoir simulator used

for full scale modelling. Impact of porosity and permeability heterogeneity impact on displacement front are evaluated and analyzed.

Future research will build on the knowledge gained here, including investigating capillary scaling techniques for heterogeneous domains, incorporating hysteresis and mineralization effects, and upscaling trapping behavior to reservoir dimensions.

6 References

Introduction:

- 1. Archer, D., Eby, M., Brovkin, V., Ridgwell, A., Cao, L., Mikolajewicz, U., Caldeira, K., Matsumoto, K., Munhoven, G., Montenegro, A. and Tokos, K., 2009. Atmospheric lifetime of fossil fuel carbon dioxide. *Annual Review of Earth and Planetary Sciences*, 37, pp.117–134. https://doi.org/10.1146/annurev.earth.031208.100206
- Bachu, S., 2008. CO₂ storage in geological media: Role, means, status and barriers to deployment. *Progress in Energy and Combustion Science*, 34(2), pp.254–273. https://doi.org/10.1016/j.pecs.2007.10.001
- 3. Benson, S.M. and Cole, D.R., 2008. Co₂ sequestration in deep sedimentary formations. *Elements*, 4(5), pp.325–331. https://doi.org/10.2113/gselements.4.5.325
- 4. Friedlingstein, P., Jones, M.W., O'Sullivan, M. *et al.*, 2022. Global carbon budget 2022. *Earth System Science Data*, 14(11), pp.4811–4900. https://doi.org/10.5194/essd-14-4811-2022
- 5. IEAGHG (IEA Greenhouse Gas R&D Programme), 2021. *CO₂ Storage Resources and Their Uncertainty* (overview of global storage potential). Executive summary and reports available at: https://ieaghg.org/publications/technical-reports
- 6. IPCC, 2005. Special Report on Carbon Dioxide Capture and Storage. Cambridge University Press for the Intergovernmental Panel on Climate Change. Full report: IPCC- Intergovernmental Panel on Climate Change
- 7. IPCC, 2021. Climate Change 2021: The Physical Science Basis. Contribution of Working Group I to the Sixth Assessment Report (AR6). Cambridge University Press. Summary for Policymakers: https://www.ipcc.ch/report/ar6/wg1/
- 8. NOAA Global Monitoring Laboratory, 2024. Trends in atmospheric carbon dioxide (global mean, ~420+ ppm in 2024). National Oceanic and Atmospheric Administration. https://gml.noaa.gov/ccgg/trends/
- 9. Paris Agreement, 2015. *United Nations Framework Convention on Climate Change (UNFCCC)*. Text of the Agreement: https://unfccc.int/process-and-meetings/the-parisagreement/the-parisagreement
- 10. Lord, A.S., Kobos, P.H. and Borns, D.J., 2014. Geologic storage of hydrogen: Scaling up to meet city transport needs. *International Journal of Hydrogen Energy*, 39(28), pp.15570–15582. https://doi.org/10.1016/j.ijhydene.2014.07.121
- 11. Katz, D.L. and Tek, M.R., 1981. *Underground Storage of Fluids*. Ann Arbor Science Publishers. Google Books: https://books.google.com/books?id=VxQSAQAAIAAJ

12. Holm, L.W. and Josendal, V.A. 1974. Mechanisms of Oil Displacement by Carbon Dioxide. *J Pet Technol* 26 (12): 1427–1438. SPE-4736-PA. https://doi.org/10.2118/4736-PA

State of the art:

- 13. Aziz, K. & Settari, A. (1979). *Petroleum Reservoir Simulation*. Applied Science Publishers.
- 14. Bear, J. (1972). Dynamics of Fluids in Porous Media. Dover Publications.
- 15. Blunt, M.J. (2017). *Multiphase Flow in Permeable Media: A Pore-Scale Perspective*. Cambridge University Press. https://doi.org/10.1017/9781316145098
- 16. Chen, Z., Huan, G. & Ma, Y. (2006). Computational Methods for Multiphase Flows in Porous Media. SIAM. https://doi.org/10.1137/1.9780898718942
- 17. Flemisch, B. et al. (2011). DuMuX: DUNE for multi-{phase, component, scale, physics, domain} flow and transport in porous media. *Advances in Water Resources*, 34(9), 1102–1112. https://doi.org/10.1016/j.advwatres.2011.03.007
- 18. Horgue, P., Augier, F., Debenest, G. & Quintard, M. (2015). A two-phase flow solver based on a volume-of-fluid technique for interfacial flows in complex geometries. *Computers & Fluids*, 94, 69–84. https://doi.org/10.1016/j.compfluid.2014.11.017
- 19. Lie, K.-A. (2019). *An Introduction to Reservoir Simulation Using MATLAB/GNU Octave: MRST*. Cambridge University Press. https://doi.org/10.1017/9781108591416
- 20. Rock Flow Dynamics (2024). tNavigator® User Manual CO2STORE Module.
- 21. CMG (2024). GEM Compositional Simulator User Guide. https://www.cmgl.ca/software/gem
- 22. SLB (2024). *ECLIPSE Technical Description*. https://www.software.slb.com/products/eclipse
- 23. Honarpour, M., Koederitz, L. & Harvey, A.H. (1986). *Relative Permeability of Petroleum Reservoirs*. CRC Press. https://doi.org/10.1201/9781315138770
- 24. Jackson, S.J., Reynolds, C.A., Schembre-Miller, J. & Krevor, S. (2018). Characterization of multiphase flow in heterogeneous rocks using X-ray micro-CT at reservoir conditions. *Water Resources Research*, 54(4), 3132–3148. https://doi.org/10.1029/2017WR022282
- 25. Krevor, S. et al. (2012). Capillary heterogeneity trapping of CO₂ in sandstone rock at reservoir conditions. *Geophysical Research Letters*, 39(15), L15401. https://doi.org/10.1029/2012GL052008
- 26. Pentland, C.H., El-Mohtar, C., Iglauer, S. & Blunt, M.J. (2011). Measurement of non-wetting phase trapping in sandstones and sandpacks. *Water Resources Research*, 47(8), W08531. https://doi.org/10.1029/2010WR009874
- 27. Modeling and investigation of the influence of capillary heterogeneity on multiphase flow of CO₂ and brine (2012). *Water Resources Research*, 48(8), W08519. https://doi.org/10.1029/2011WR011212
- 28. Benson, S.M. & Cole, D.R. (2008). CO₂ sequestration in deep sedimentary formations. *Elements*, 4(5), 325–331. https://doi.org/10.2113/gselements.4.5.325
- 29. Brooks, R.H. & Corey, A.T. (1966). *Properties of porous media affecting fluid flow*. Colorado State University Hydrology Paper No. 3.
- 30. Corey, A.T. (1954). The interrelation between gas and oil relative permeabilities. *Petroleum Transactions*, *AIME*, 225, 129–134.
- 31. Land, C.S. (1968). Calculation of imbibition relative permeability from rock properties. *SPE Journal*, 8(2), 149–156. SPE-1942-PA. https://doi.org/10.2118/1942-PA

- 32. Killough, J.E. (1976). Reservoir simulation with history-dependent saturation functions. *SPE Journal*, 16(1), 37–48. SPE-5106-PA. https://doi.org/10.2118/5106-PA
- 33. Leverett, M.C. (1941). Capillary behavior in porous solids. *Transactions of the AIME*, 142(1), 152–169. https://doi.org/10.2118/941152-G
- 34. Jackson, S.J., Lin, Q. & Krevor, S. (2020). Representative elementary volumes, hysteresis, and heterogeneity in multiphase flow of CO₂—brine. *Water Resources Research*, 56(10), e2019WR026396. https://doi.org/10.1029/2019WR026396
- 35. Bachu, S. (2008). CO₂ storage in geological media: Role, means, status and barriers to deployment. *Progress in Energy and Combustion Science*, 34(2), 254–273. https://doi.org/10.1016/j.pecs.2007.10.001
- 36. Gaus, I. (2010). Role and impact of CO₂–rock interactions during CO₂ storage in sedimentary rocks. *International Journal of Greenhouse Gas Control*, 4(1), 73–89. https://doi.org/10.1016/j.ijggc.2009.09.015
- 37. Peng, D.Y. & Robinson, D.B. (1976). A new two-constant equation of state. *Industrial & Engineering Chemistry Fundamentals*, 15(1), 59–64. https://doi.org/10.1021/i160057a011
- 38. Krevor, S. et al. (2015). Experimental and numerical investigation of residual trapping in Bentheimer sandstone. *International Journal of Greenhouse Gas Control*, 42, 1–17. https://doi.org/10.1016/j.ijggc.2015.08.007

Methodology:

- 39. Blunt, M.J. (2017) *Multiphase Flow in Permeable Media: A Pore-Scale Perspective*. Cambridge: Cambridge University Press. https://doi.org/10.1017/9781316145098
- 40. Krevor, S., Pini, R., Zuo, L. & Benson, S.M. (2012) 'Capillary heterogeneity trapping of CO₂ in a sandstone rock at reservoir conditions', *Geophysical Research Letters*, 39(15), L15401. https://doi.org/10.1029/2012GL052008
- 41. Pentland, C.H., El-Mohtar, C., Iglauer, S. & Blunt, M.J. (2011) 'Measurement of non-wetting phase trapping in sandstones and sandpacks', *Water Resources Research*, 47(8), W08531. https://doi.org/10.1029/2010WR009874
- 42. Lie, K.-A. (2019) An Introduction to Reservoir Simulation Using MATLAB/GNU Octave: User Guide for the MRST. Cambridge: Cambridge University Press. https://doi.org/10.1017/9781108591416
- 43. API (1998) Recommended Practices for Core Analysis Procedures (API RP 40). American Petroleum Institute. Catalog page: https://www.api.org/products-and-services/standards (search: "RP 40 Core Analysis")
- 44. Lake, L.W. (1989) *Enhanced Oil Recovery*. Englewood Cliffs: Prentice Hall. (Overview page: https://www.pearson.com/en-us/subject-catalog/p/enhanced-oil-recovery/P20000006715/)
- 45. Jackson, S.J., Reynolds, C.A., Schembre-Miller, J. & Krevor, S. (2018) 'Characterization of multiphase flow in heterogeneous rocks using X-ray micro-CT at reservoir conditions', *Water Resources Research*, 54(4), 3132–3148. https://doi.org/10.1029/2017WR022282

Results:

46. Peysson, Y., André, L., & Azaroual, M. (2014). Well injectivity during CO₂ storage operations in deep saline aquifers – Part 1: Experimental investigation of drying effects, salt precipitation and capillary forces. *International Journal of Greenhouse Gas Control*, 22, 291–300. https://doi.org/10.1016/j.ijggc.2013.10.031

7 Appendix A: MATlab code

```
% Simulation of CO2 injection in a cylindrical rock sample
% INCLUDE packs for S1/S2/S3
% Scenarios:
  S1: Homogeneous plug (uniform PORO/PERM)
   S2: Heterogeneous plug (random PORO)
   S3: Heterogeneous plug (random PERM)
   S4: Heterogeneous plug (random PORO/PERM)
% What is written per scenario folder (./case S1, ./case S2, ./case S3):
                   (keyword: ACTNUM)
  ACTNUM.inc
%
  PORO.inc
                   (keyword: PORO)
%
                   (keyword: PERMX) [PERMY=PERMX, PERMZ=0.1*PERMX if needed]
  PERMX.inc
  WELLSPECS.inc
                   (header: WELLSPECS, lines: 'WELL' FIELD i j /)
  COMPDAT.inc
                   (header: COMPDAT, single-layer completion: k=k1=k2)
                   (header: WINJGAS, lines: 'INJ#' STREAM 'INJGAS' /)
  WINJGAS.inc
  WCONINJE.inc
                   (header: WCONINJE, lines: 'INJ#' 'GAS' 'OPEN' 'RATE' 1E-2 1E-2
220.0 2* /)
  WCONPROD.inc
                   (header: WCONPROD, lines: 'PROD#' 'OPEN' 'BHP' 5* 150 /)
%
% Notes
% - Pc includes are optional here; placeholders exist (disabled by default).
function generate_inc_packs1()
clc; fprintf('=== Generating INCLUDE packs for S1 (Homog), S2 (Het), S3 (Het+local Pc)
===\n');
%% ------ GRID ------
dx = 2; dy = 2; dz = 2; % [mm]
Nx = 76/dx; Ny = 76/dy; Nz = 70/dz; % 38x38x35
Lx = Nx*dx; Ly = Ny*dy;
                               % [mm]
radius_mm = 38/2;
                                % [mm]
% Cylinder ACTNUM (1=active)
ACTNUM = ones(Nx,Ny,Nz,'uint8');
xc = Lx/2; yc = Ly/2;
for i = 1:Nx
   for j = 1:Ny
       x = (i-0.5)*dx; y = (j-0.5)*dy;
       if ~is_inside_cylinder(x,y,xc,yc,radius_mm)
          ACTNUM(i,j,:) = 0;
       end
   end
visualize_cylinder_combined(ACTNUM, dx, dy, dz);
%% ------ Scenarios ------
scenarios = {
struct('id','S1','name','Homogeneous','phi mu',0.20,'phi sigma',0.0,'k mu',100,'k sigma'
,0.0), \dots
```

```
struct('id','S2','name','Heterogeneous
poro', 'phi_mu', 0.20, 'phi_sigma', 0.02, 'k_mu', 100, 'k_sigma', 10), ...
  struct('id','S3','name','Heterogeneous
perm','phi_mu',0.20,'phi_sigma',0.02,'k_mu',100,'k_sigma',10)
};
rng(1234);
for s = 1:numel(scenarios)
   S = scenarios{s};
    cdir = fullfile('.', ['case_' S.id]);
    if ~exist(cdir,'dir'), mkdir(cdir); end
    fprintf(' -> Writing %s (%s) in %s\n', S.id, S.name, cdir);
   % ---- ACTNUM (scenario-suffixed) ----
   write_numeric_inc(fullfile(cdir, sprintf('ACTNUM_%s.inc', S.id)), ...
                      'ACTNUM', ACTNUM, Nx, Ny, Nz);
   % ---- PORO / PERMX (scenario-suffixed) ----
    [PORO, PERMX] = make_poroperm_correlated(ACTNUM, S.phi_mu, S.phi_sigma, S.k_mu,
S.k_sigma, 0.7);
   write por perm exact(fullfile(cdir, sprintf('PORO %s.inc', S.id)), 'PORO', PORO,
Nx);
   write por perm exact(fullfile(cdir, sprintf('PERMX %s.inc', S.id)), 'PERMX', PERMX,
Nx);
   % ---- Wells (scenario-suffixed) ----
    [injIJ, prodIJ] = top bottom indices(ACTNUM);
    write_wellspecs(fullfile(cdir, sprintf('WELSPECS_%s.inc', S.id)), injIJ, prodIJ);
   write compdat (fullfile(cdir, sprintf('COMPDAT %s.inc',
                                                              S.id)), injIJ, prodIJ,
   write_WINJGAS(fullfile(cdir, sprintf('WINJGAS_%s.inc',
                                                              S.id)), size(injIJ,1));
   write wconinje(fullfile(cdir, sprintf('WCONINJE %s.inc',
                                                            S.id)), size(injIJ,1));
   write_WCONPROD(fullfile(cdir, sprintf('WCONPROD_%s.inc', S.id)), size(prodIJ,1));
end
fprintf('All INCLUDE packs done.\n');
end
% ========= helpers ===========
function visualize_cylinder_combined(ACTNUM, dx, dy, dz, strideI, strideJ, planesK)
   % ----- defaults -----
   if nargin < 5 || isempty(strideI), strideI = 2; end</pre>
    if nargin < 6 || isempty(strideJ), strideJ = 2; end</pre>
    [Nx,Ny,Nz] = size(ACTNUM);
    if nargin < 7 || isempty(planesK), planesK = 1:Nz; end</pre>
   % ----- coordinates -----
   xc = ((1:Nx)-0.5)*dx;
                                   % x centers (i)
   yc = ((1:Ny)-0.5)*dy;
                                   % y centers (j)
                                  % z centers (k)
   zc = ((1:Nz)-0.5)*dz;
    [Xm, Ym, Zm] = meshgrid(xc, yc, zc); % size [Ny x Nx x Nz]
   Vm = permute(smooth3(double(ACTNUM), 'box', 3), [2 1 3]);
```

```
% ----- figure -----
figure('Color','w','Name','Plug3D');
p = patch(isosurface(Xm, Ym, Zm, Vm, 0.5));
isonormals(Xm, Ym, Zm, Vm, p);
set(p, 'FaceColor',[0.78 0.82 0.92], 'EdgeColor', 'none', 'FaceAlpha', 0.18); hold on;
% end caps
c = patch(isocaps(Xm, Ym, Zm, Vm, 0.5));
set(c, 'FaceColor', [0.90 0.92 0.97], 'EdgeColor', 'none', 'FaceAlpha', 0.25);
axis equal; grid on; box on;
x\lim([\min(xc)-dx/2, \max(xc)+dx/2]);
ylim([min(yc)-dy/2, max(yc)+dy/2]);
zlim([min(zc)-dz/2, max(zc)+dz/2]);
xlabel('x [mm]'); ylabel('y [mm]'); zlabel('z [mm]');
view(35,20); camlight headlight; lighting gouraud;
% ----- internal wireframe ------
linecol = [0.25 \ 0.25 \ 0.25];
for kk = planesK(:).'
    % I-lines on plane k = kk
    for j = 1:strideJ:Ny
        maskI = find(ACTNUM(:,j,kk)==1);
        if numel(maskI) >= 2
            xi = (maskI-0.5)*dx;
            yi = (j-0.5)*dy * ones(size(maskI));
            zi = (kk-0.5)*dz * ones(size(maskI));
            plot3(xi, yi, zi, '-', 'Color', linecol, 'LineWidth', 0.6);
        end
    end
    % J-lines on plane k = kk
    for i = 1:strideI:Nx
        maskJ = find(ACTNUM(i,:,kk)==1);
        if numel(maskJ) >= 2
            xj = (i-0.5)*dx * ones(size(maskJ));
            yj = (maskJ-0.5)*dy;
            zj = (kk-0.5)*dz * ones(size(maskJ));
            plot3(xj, yj, zj, '-', 'Color', linecol, 'LineWidth', 0.6);
        end
    end
end
% ----- well markers -----
% top injectors (k=1)
[Ii,Ji] = find(ACTNUM(:,:,1)==1);
if ~isempty(Ii)
    xi = (Ii-0.5)*dx; yi = (Ji-0.5)*dy; zi = ones(size(Ii))*0.5*dz;
    plot3(xi, yi, zi, 'o', 'MarkerSize',5, ...
        'MarkerFaceColor',[0 0.45 1], 'MarkerEdgeColor','k');
end
% bottom producers (k=Nz)
[Ip,Jp] = find(ACTNUM(:,:,Nz)==1);
if ~isempty(Ip)
    xp = (Ip-0.5)*dx; yp = (Jp-0.5)*dy; zp = ones(size(Ip))*(Nz-0.5)*dz;
    plot3(xp, yp, zp, '^', 'MarkerSize',5, ...
```

```
'MarkerFaceColor',[1 0.45 0], 'MarkerEdgeColor','k');
    end
title('Cylindrical plug with internal wireframe & well locations', 'FontWeight', 'bold');
% dummy plot handles to control legend icons
hSurface = plot3(nan,nan,nan,'s','MarkerFaceColor',[0.78 0.82
0.92], 'MarkerEdgeColor', 'none');
           = plot3(nan,nan,nan,'s','MarkerFaceColor',[0.90 0.92
0.97], 'MarkerEdgeColor', 'none');
           = plot3(nan,nan,nan,'-','Color',[0.25 0.25 0.25],'LineWidth',0.6);
hWire
           = plot3(nan,nan,nan,'o','MarkerFaceColor',[0 0.45 1],'MarkerEdgeColor','k');
hInj
           = plot3(nan,nan,'^','MarkerFaceColor',[1 0.45 0],'MarkerEdgeColor','k');
hProd
legend([hSurface, hCaps, hWire, hInj, hProd], ...
    {'Plug surface', 'End caps', 'Internal wireframe', 'Injectors (top)', 'Producers
(bottom)'}, ...
    'Location', 'northeastoutside');
end
function write_por_perm_exact(filename, keyword, A3, Nx)
    fid = fopen(filename, 'w');
    assert(fid>0, 'Cannot open %s', filename);
    fprintf(fid, '%s\n', keyword);
                                    % header (PORO or PERMX)
    v = reshape(A3, [], 1);
                                           % flatten I-fast (i fastest)
    n = numel(v);
    for t = 1:n
        fprintf(fid, ' %12.6f', v(t));
                                         % fixed width 12.6f
        if mod(t, Nx) == 0
            fprintf(fid, '\n');
                                            % break after Nx values
        end
    end
    if mod(n, Nx) \sim = 0
        fprintf(fid, '\n');
    end
    fprintf(fid, '/\n');
                                          % closing slash on its own line
    fclose(fid);
end
function inside = is_inside_cylinder(x,y,xc,yc,R)
    dx = x-xc; dy = y-yc; inside = (dx*dx + dy*dy) <= R*R;
end
function writeText(filename, s)
    fid = fopen(filename,'w'); assert(fid>0, 'Cannot open %s', filename);
    fprintf(fid, '%s', s); fclose(fid);
end
function write_numeric_inc(filename, keyword, A, Nx, Ny, Nz)
    fid = fopen(filename, 'w'); assert(fid>0, 'Cannot open %s', filename);
    fprintf(fid, '%s\n', keyword);
                                                  % header + NEWLINE
    % I-fast order
    for k = 1:Nz
        for j = 1:Ny
```

```
for i = 1:Nx
                v = A(i,j,k);
                if isinteger(v) || islogical(v)
                    fprintf(fid, '%d ', v);
                else
                    fprintf(fid, '%12.6f ', v);
                end
            end
            fprintf(fid, '\n');
        end
    end
    fprintf(fid, '/\n');
    fclose(fid);
end
function [PORO, PERMX] = make poroperm correlated(ACTNUM, phi mu, phi sigma, k mean md,
k std md, rho)
    % rho in [-0.99, 0.99]
    rho = \max(\min(\text{rho}, 0.99), -0.99);
    [Nx,Ny,Nz] = size(ACTNUM);
    N = Nx*Ny*Nz;
    msk = ACTNUM(:)==1;
    % --- 1) Porosity (Gaussian, clipped to [0,1])
    zphi = zeros(N,1); zphi(msk) = randn(nnz(msk),1);
    phi = phi_mu + phi_sigma * zphi;
    phi = max(0, min(1, phi));  % clip
    PORO = reshape(phi, [Nx,Ny,Nz]);
    % --- 2) Target lognormal parameters for k (mD)
    sig lk = sqrt(log(1 + (k std md/k mean md)^2));
    mu_lk = log((k_mean_md^2) / sqrt(k_std_md^2 + k_mean_md^2));
    % --- 3) Correlated driver for log-k
    z2 = zeros(N,1); z2(msk) = randn(nnz(msk),1);
    zk = rho * zphi + sqrt(1 - rho^2) * z2;
    % --- 4) Build k (lognormal) and floor it
    logk = mu lk + sig lk * zk;
    kmd = zeros(N,1); kmd(msk) = exp(logk(msk));
                                                           % mD
    kmd = max(kmd, 1e-3);
                                                           % floor
    PERMX = reshape(kmd, [Nx,Ny,Nz]);
end
function [injIJ, prodIJ] = top_bottom_indices(ACTNUM)
    [Nx,Ny,Nz] = size(ACTNUM);
    inj = []; prod = [];
    for i = 1:Nx
      for j = 1:Ny
        if ACTNUM(i,j,1)==1, inj = [inj; i j]; end
        if ACTNUM(i,j,Nz)==1, prod = [prod; i j]; end
      end
    end
    injIJ = inj;
```

```
prodIJ = prod;
end
function write_wellspecs(filename, injIJ, prodIJ)
    fid = fopen(filename, 'w');
    assert(fid>0, 'Cannot open %s', filename);
    fprintf(fid, 'WELSPECS\n');
    % Injectors
    for n = 1:size(injIJ,1)
        i = injIJ(n,1); j = injIJ(n,2);
        fprintf(fid, ' ''INJ%d'' ''FIELD'' %3d %3d /\n', n, i, j);
    end
    % Producers
    for n = 1:size(prodIJ,1)
        i = prodIJ(n,1); j = prodIJ(n,2);
        fprintf(fid, ' ''PROD%d'' ''FIELD'' %3d %3d /\n', n, i, j);
    end
    fprintf(fid, '/\n');
    fclose(fid);
end
function write_compdat(filename, injIJ, prodIJ, Nz)
    fid = fopen(filename, 'w');
    assert(fid > 0, 'Cannot open %s', filename);
    fprintf(fid, 'COMPDAT\n');
    % Injectors (top layer, k=1)
    for n = 1:size(injIJ,1)
        i = injIJ(n,1);
        j = injIJ(n,2);
fprintf(fid, ' ''INJ%d''
                                    %3d %3d
                                                %3d
                                                      %3d ''OPEN'' 2* 0.0006 1* 0.0
/\n', ...
            n, i, j, 1, 1);
    end
    % Producers (bottom layer, k=Nz)
    for n = 1:size(prodIJ,1)
        i = prodIJ(n,1);
        j = prodIJ(n,2);
fprintf(fid, ' ''PROD%d'' %3d %3d %3d %3d ''OPEN'' 2* 0.0006 1* 0.0
/\n', ...
            n, i, j, Nz, Nz);
    end
    fprintf(fid, '/\n');
    fclose(fid);
end
function write_WINJGAS(filename, Nin)
    fid = fopen(filename,'w'); assert(fid>0, 'Cannot open %s', filename);
    fprintf(fid, 'WINJGAS\n');
    for n = 1:Nin
        fprintf(fid, ' ''INJ%d'' STREAM ''INJGAS'' /\n', n);
```

```
end
    fclose(fid);
end
function write wconinje(filename, Nin)
    fid = fopen(filename,'w'); assert(fid>0, 'Cannot open %s', filename);
    fprintf(fid, 'WCONINJE\n');
    for n = 1:Nin
        fprintf(fid, '''INJ%d'' ''GAS'' ''OPEN'' ''BHP'' 1* 1* 220.0 2* /\n', n);
    fprintf(fid, '/\n');
    fclose(fid);
end
function write WCONPROD(filename, Np)
    fid = fopen(filename, 'w'); assert(fid>0, 'Cannot open %s', filename);
    fprintf(fid, 'WCONPROD\n');
    for n = 1:Np
        fprintf(fid, '''PROD%d'' ''OPEN'' ''BHP'' 5* 200 /\n', n);
    fprintf(fid, '/\n');
    fclose(fid);
end
function make_hist_with_gaussian(vec, mu, sigma, xlab, ttl, outpng)
    % vec : vector of values (e.g., PERMX(active_idx))
    % mu
          : target mean
    % sigma : target std
    % xlab : x-axis label
    % ttl : plot title
    % outpng: output PNG path
    vec = vec(:);
    nbins = max(20, round(sqrt(numel(vec))));  % simple Freedman-Diaconis-ish
    f = figure('Visible', 'on', 'Color', 'w', 'Position', [80 80 880 520]);
    % Histogram (PDF)
    histogram(vec, nbins, 'Normalization', 'pdf', 'EdgeColor', [0.3 0.3 0.3]); hold on;
    % Gaussian overlay (keeping phi within [0,1] range)
    if contains(xlab, 'Porosity')
        x = linspace(max(0, mu-4*sigma), min(1, mu+4*sigma), 400);
    else
        x = linspace(mu-4*sigma, mu+4*sigma, 400);
    if sigma > 0
        g = (1/(sigma*sqrt(2*pi))) * exp(-0.5*((x-mu)/sigma).^2);
        plot(x, g, 'LineWidth', 2);
        legend({'Sampled data', 'Gaussian PDF'}, 'Location', 'best');
    else
        % sigma == 0 → target is a delta at mu; show a vertical line
        yl = ylim;
        plot([mu mu], yl, 'LineWidth', 2);
        legend({'Sampled data', sprintf('Target = %.4g', mu)}, 'Location','best');
    end
    xlabel(xlab); ylabel('Probability density'); title(ttl);
```

```
grid on; box on;

% Save @ 300 dpi
  exportgraphics(gcf, outpng, 'Resolution', 300);
  %close(gcf);
end
```

8 Appendix B: .DATA file

RUNSPEC TITLE THESIS_PLUG **METRIC START** 1 'JAN' 2019 / **RUNCTRL** DTMIN 0.00000000001 / **DIMENS** 38 38 35 / WATER GAS CO2STORE **COMPS** 2 / **WELLDIMS** 100 1 2 50 / **UNIFIN UNIFOUT**

GRID

--INCLUDE

--'PERMX_S2.inc'/

--'PERMX_S3.inc'/

NOECHO **INIT MINPV** 1e-12 DX 50540*0.002 / DY 50540*0.002 / DZ50540*0.002 / **TOPS** 1444*2000.0 / **INCLUDE** 'ACTNUM_S1.inc'/ **PORO** 50540*0.2/ --INCLUDE --'PORO_S2.inc'/ --'PORO_S3.inc'/ PERMX 50540*100.0 /

```
COPY
'PERMX' 'PERMY' /
COPY
'PERMX' 'PERMZ' /
MULTIPLY
PERMZ 0.1/
PROPS
ROCK
 1.0 1e-6 /
COREYWG
-- SWL SWU SWCR SGWCR KRGU KRG KRW KRWU PC ng nw
 0.05 1 0.25 0.08 1 0.05 0.02 1.00 0.0 2.5 3.5 *1 /
SALINITY
0.7/35-40g/1 \rightarrow 35-40g/kg \rightarrow 0.63-0.72 \text{ mol/g}
NCOMPS
2 /
CNAMES
'CO2' 'H2O'/
ZI
-- composition
0 1/
```

```
RTEMP
40
SOLUTION
EQUIL
--depth pressure WOC PCWO GOC PCGO
2000 200 1500 0 0 0 /
RPTRST
'BASIC=2' 'ALLPROPS'/
SUMMARY
WBHP
WBP
WGIR
WGIT
FGIPG
FPR
FGIT
```

```
RUNSUM
DATE
SCHEDULE
--TIME
--0.1 1 2 5 10 15 20 30 40 50 60 /
RPTRST
'BASIC=2' 'ALLPROPS'/
INCLUDE
'WELLSPECS_S1.inc' /
INCLUDE
'COMPDAT_S1.inc' /
WELLSTRE
'INJGAS' 10 /
INCLUDE
'WINJGAS_S1.inc' /
--GCONINJE
-- 'FIELD' GAS RATE 10.0 1* 1* 1* /
--/
INCLUDE
'WCONINJE_S1.inc' /
INCLUDE
```

```
'WCONPROD_S1.inc' /

/
TSTEP
60*0.000694444 / -- 1-minute tstep
/
END
```